

Enhanced shot noise in graphene quantum point contacts with electrostatic reconstruction

M. Garg,^{1,2,*} O. Maillet,^{1,†} N. L. Samuelson,³ T. Wang,^{4,5} J. Feng,⁶ L. A. Cohen,³ K. Watanabe,⁷ T. Taniguchi,⁸ P. Roulleau,^{1,‡} M. Sasseti,^{9,10} M. Zaletel,^{4,5} A. F. Young,³ D. Ferraro,^{9,10} P. Roche,¹ and F.D. Parmentier^{1,11,§}

¹*Université Paris-Saclay, CEA, CNRS, SPEC, 91191 Gif-sur-Yvette cedex, France*

²*Department of Physics, Indian Institute of Technology Roorkee, Uttarakhand 247667, India*

³*Department of Physics, University of California at Santa Barbara, Santa Barbara CA 93106, USA*

⁴*Department of Physics, University of California at Berkeley, Berkeley, CA 94720, USA*

⁵*Material Science Division, Lawrence Berkeley National Laboratory, Berkeley, CA 94720, USA*

⁶*Graduate Group in Applied Science & Technology,*

University of California, Berkeley, California 94720, USA

⁷*Research Center for Electronic and Optical Materials,*

National Institute for Materials Science, 1-1 Namiki, Tsukuba 305-0044, Japan

⁸*Research Center for Materials Nanoarchitectonics,*

National Institute for Materials Science, 1-1 Namiki, Tsukuba 305-0044, Japan

⁹*Dipartimento di Fisica, Università di Genova, Via Dodecaneso 33, 16146, Genova, Italy*

¹⁰*SPIN-CNR, Via Dodecaneso 33, 16146, Genova, Italy*

¹¹*Laboratoire de Physique de l'École normale supérieure, ENS, Université PSL,*

CNRS, Sorbonne Université, Université Paris Cité, F-75005 Paris, France

(Dated: March 24, 2025)

Shot noise measurements in quantum point contacts are a powerful tool to investigate charge transport in the integer and fractional quantum Hall regime, in particular to unveil the charge, quantum statistics and tunneling dynamics of edge excitations. In this letter, we describe shot noise measurements in a graphene quantum point contact in the quantum Hall regime. At large magnetic field, the competition between confinement and electronic interactions gives rise to a quantum dot located at the saddle point of the quantum point contact. We show that the presence of this quantum dot leads to a 50–100 % increase in the shot noise, which we attribute to correlated charge tunneling. Our results highlight the role played by the electrostatic environment in those graphene devices.

Quantum point contacts (QPCs) are a staple of mesoscopic quantum physics, bringing forth the demonstration of noiseless electron flow in ballistic conductors [1], as well as the observation of fractional electron charges [2–5], including anyonic statistics [6,7] and their scaling dimension [8,9] through noise measurements. Implementing QPCs in graphene has long been an exciting prospect due to its rich quantum Hall (QH) physics, particularly the presence of robust odd- and even-denominator fractional QH states [10–12]. QPCs have recently been implemented in hexagonal boron nitride (hBN)-encapsulated graphene to realize quantum Fabry-Perot interferometers [13,14], which has led to the demonstration of anyonic statistics in graphene using similar devices in the fractional QH regime [15,16]. Contrary to GaAs 2DEGs, where the metallic gates of the QPC tend to degrade the electron mobility in the QPC vicinity due to strain [17], the cleanest graphene QPC devices are made with tailored few layered graphite gates [18], which greatly enhance the mobility [12], allowing the precise characterization of the scaling laws predicted by Tomonaga-Luttinger liquids theory for tunneling into a fractional QH edge channel [19]. However, at high magnetic field, the combination of low disorder and strong Coulomb interaction can induce electrostatic reconstruction, whereby locally increasing the carrier density at the QPC saddle point becomes energetically favor-

able [20]. This leads to the formation of a quantum dot which will dictate the transport properties of the QPC. In particular, the shot noise is likely to be affected by the presence of the quantum dot, potentially affecting ‘collider’-type experiments where quantum statistics of the carriers are obtained from the shot noise [1,6]. In this letter, we investigate the shot noise of a graphene QPC in the QH regime in presence of reconstruction at the QPC saddle point. We show that the formation of the reconstructed quantum dot leads to a significant increase in the shot noise. We explain this increase by the presence of several edge channels circulating in the quantum dot: Coulomb interactions coupling neighboring channels induce correlations between successive tunneling events across the dot. These memory effects in the charge transfers are characterized by an enhanced shot noise.

Fig. 1a) shows an optical micrograph of the sample, described in details in [18]. The QPC is realized by the joint operation of a global graphite back gate (upon which a voltage V_B is applied) and a graphite top gate divided in four regions: east (E) - west (W), which tune the filling factor ν_{EW} in the bulk, and north (N) - south (S), which tune the filling factor ν_{NS} below the QPC gates. Each pair of gates (E-W, and N-S) is controlled by a single gate voltage: V_{EW} and V_{NS} . At $B = 13$ T, V_B and V_{NS} are set to values such that $\nu_{NS} = 0$, and V_{EW} is swept along the $\nu_{EW} = 2$ plateau, with edge channels flowing clockwise

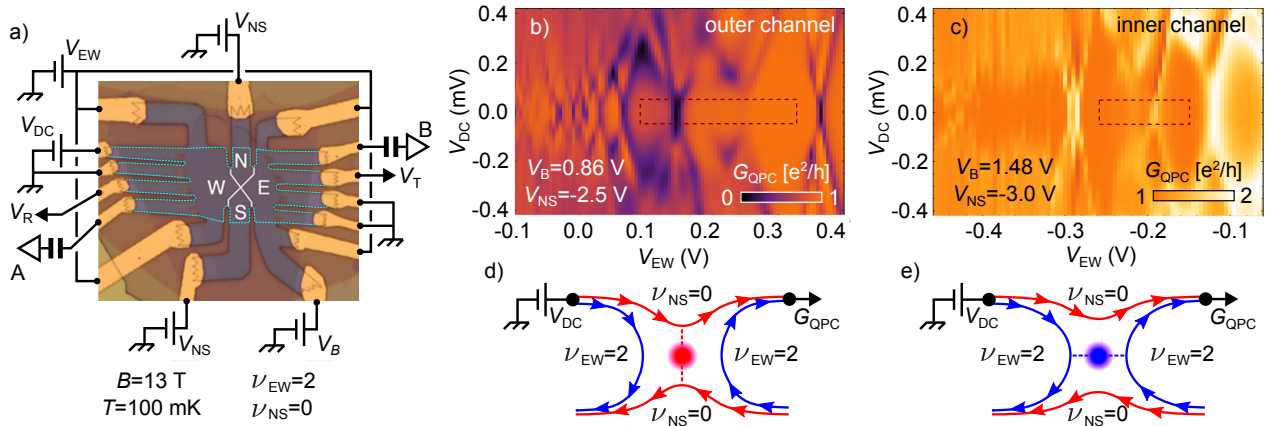


Figure 1. (a), Sample micrograph, indicating the measurement wiring. The dashed white lines indicate the edges of the graphene flake. (b) and (c), Conductance across the QPC measured as a function of the bias voltage V_{DC} and the east and west gate voltage V_{EW} , for two settings of the back and north/south gate voltages. The red dashed rectangles indicate the regions corresponding to the data shown in Fig. 2. (d) and (e), Schematic representations of the edge channels configuration at the QPC corresponding to the data shown in (b) and (c), respectively. Red arrow: outer edge channel. Blue arrow: inner edge channel.

along the edges of the sample. A DC voltage V_{DC} , along with a small AC excitation δV_{AC} (not shown in Fig. 1a) are applied to the upper left contact, and the shot noise is measured on two lines (A and B) on both sides of the sample, in auto- and cross-correlations. Transmitted and reflected differential conductances $e^2/h \times dV_{T,R}/\delta V_{AC}$ are detected on contacts downstream of the noise measurement contacts. The next contacts are connected to a cold ground. The electron density close to the contacts is tuned using the low-resistivity silicon back gate embedded in the substrate, such that there is no reflection at the contacts connected to the cold ground. In all measurements shown here, the dilution refrigerator temperature was fixed and regulated to 100 mK.

The conductance versus east-west gate voltage and DC voltage maps shown in Fig. 1b) and c) highlight the two operational settings of the device in which we performed noise measurements, corresponding to a QPC conductance $G_{QPC} = e^2/h \times dV_T/\delta V_{AC}$ ranging between $\{0-1\}e^2/h$ (Fig. 1b), and $\{1-2\}e^2/h$ (Fig. 1c). Both maps show clear Coulomb diamonds features, as previously reported for these devices, that correspond to the formation of a quantum dot at the QPC saddle point due to electrostatic reconstruction. Remarkably, the resonances in the Coulomb diamonds correspond to a pinch-off of the QPC (both edge channels fully reflected) in Fig. 1b): $G_{QPC} \rightarrow 0$, and to a full opening (both edge channels fully transmitted) in Fig. 1c): $G_{QPC} \rightarrow 2e^2/h$. In both cases, G_{QPC} is quantized to $1 \times e^2/h$ inside the diamonds, which we interpret as the outer edge channel being fully transmitted, while the inner one is fully reflected. As we show below, our noise measurements confirm this interpretation. From this we infer that the quantum dot only couples to a single channel at a time (outer one in Fig. 1b),

inner one in Fig. 1c), and that the coupling changes direction between the two channels, as shown in Figs. 1d) and e). The *outer* channel is coupled in *reflection*: electrons flowing through the quantum dot are reflected at the QPC (Figs. 1d). The *inner* channel is coupled in *transmission*: electrons flowing through the quantum dot are transmitted through the QPC (Figs. 1e).

Fig. 2a) shows the dependence of the transmitted (blue) and reflected (red) differential conductances, in units of e^2/h with V_{EW} , in the regions delimited with dashed red lines in Fig. 1b) and c). In the left panel (corresponding to Fig. 1b), the transmitted conductance varies continuously between 0 and 1, while the reflected conductance varies, in a symmetric fashion, between 2 and 1. In the right panel, this behavior is inverted, with the transmitted and reflected conductances varying between 1 and 2, and 1 and 0, respectively. Importantly, in both panels, the two conductances show equal quantization at 1, over significant ranges of V_{EW} corresponding to the Coulomb diamonds in Fig. 1b) and d). Moreover, their sum (green) is constant and quantized to the Hall conductance $2 \times e^2/h$ over the whole range of V_{EW} . This indicates that charge transport is entirely mediated by the two edge channels, and that the QPC allows fully separating them. Comparing zero bias (full lines) and finite bias ($V_{DC} = 50 \mu V$, dashed lines) shows that the energy dependence of the QPC transmission is weak in this range.

The noise measurements performed in these two spans of gate and bias voltages are plotted in Fig. 2b), as a function of the transmitted DC current $I_T = \int_0^{V_{DC}} G_{QPC}(V) dV$. The excess noise ΔS generated by partitioning at the QPC is extracted from the difference between auto- and cross-correlations [21]. The experi-

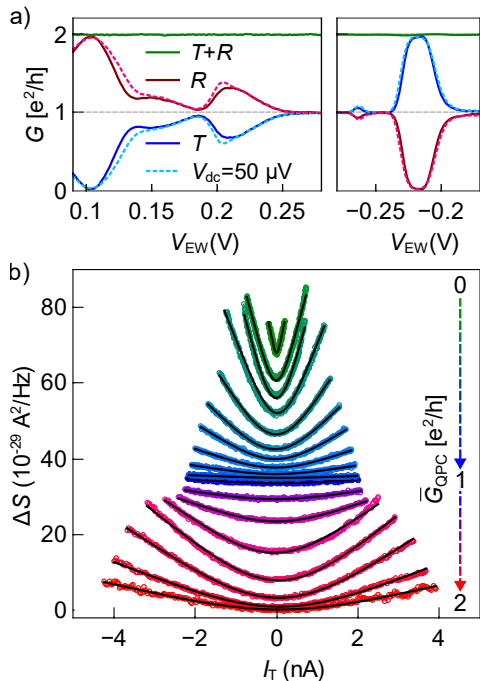


Figure 2. (a), low-energy differential conductances (see text) measured as a function of the east and west gate voltage V_{EW} , corresponding to the areas framed by the dashed lines in Fig. 1b) (left panel) and Fig. 1c) (right panel). Blue (resp. red): transmitted (resp. reflected) conductance. Green: sum of the transmitted and reflected conductances. Full lines: conductances at $V_{dc} = 0$; dashed lines: conductances at $V_{dc} = 50 \mu\text{V}$. (b), excess shot noise ΔS versus transmitted DC current I_T . Symbols: experimental data taken in the regions shown in (a), for average QPC conductances (indicated by the dashed arrow on the right) ranging from ~ 0 (green) to $\sim 2e^2/h$ (red). The curves are shifted vertically for clarity. Black lines: fits with the Fano factor as a fitting parameter.

experimental data is shown as symbols. Each curve (shifted vertically for clarity) corresponds to a fixed V_{EW} ; the symbol color indicates the average QPC conductance \bar{G}_{QPC} over the I_T range, in units of e^2/h (green: ≈ 0 , blue: 1, red: ≈ 2). Qualitatively, the data displays the behavior expected for a QPC: ΔS increases with $|I_T|$, with a slope modulated by \bar{G}_{QPC} . In particular, for \bar{G}_{QPC} between 0 and 1 (green to blue), corresponding to the configuration of Fig. 1b) and d) where the outer channel is partitioned through the QPC, the slope decreases monotonously with \bar{G}_{QPC} , and vanishes at $\bar{G}_{QPC} = 1$. For \bar{G}_{QPC} between 1 and 2 (blue to red), corresponding to the configuration of Fig. 1c) and e) where the inner channel is partitioned through the QPC, the slope is maximum at intermediate \bar{G}_{QPC} , and again decreases as $\bar{G}_{QPC} \rightarrow 2$. We analyzed quantitatively our data by fitting it with the finite temperature excess shot noise formula [21,22]:

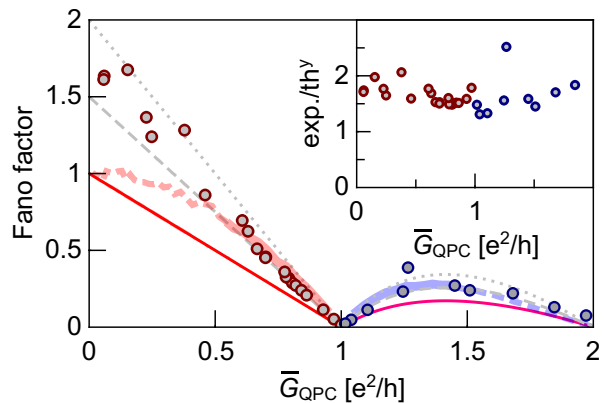


Figure 3. Fano factor versus QPC conductance. Symbols: values extracted from the fits shown in Fig. 2b) (red: outer channel, blue: inner channel). The solid, dashed and dotted lines are the Fano factor predictions with respective prefactors $\alpha = 1, 1.5$ and 2 . The thick lines are the results of the semiclassical model (see text). Inset: ratio between extracted Fano factor and Eq. 2 with $\alpha = 1$, as a function of the QPC conductance.

$$\Delta S = 2eF \left(I_T \times \coth\left(\frac{eI_T}{2\bar{G}_{QPC}k_B T}\right) - 2\bar{G}_{QPC} \frac{k_B T}{e} \right), \quad (1)$$

with the Fano factor F as the only fit parameter, \bar{G}_{QPC} and $T = 100 \text{ mK}$ being fixed. The fits are plotted as black lines in Fig. 2b) (also shifted vertically for clarity), and show a very good agreement with the measurement data.

The extracted values of F are plotted in Fig. 3 as a function of \bar{G}_{QPC} . They match well the expected behavior of a QPC sequentially transmitting two channels with respective transmissions τ_1 and τ_2 :

$$F = \alpha \left((1 - \tau_1) + \frac{\tau_2(1 - \tau_2)}{1 + \tau_2} \right), \quad (2)$$

albeit with a prefactor α markedly larger than 1: $\alpha \approx 1.5 - 2$, see inset of Fig. 3. The typical uncertainty on the extraction of F , corresponding to the size of the symbols, is much smaller than the difference between the curve for $\alpha = 1$ (full lines) and that for $\alpha = 1.5$ (dashed lines). This 1.5 - 2 prefactor is observed regardless of the way one calculates and plots the Fano factor for each channel, with very similar results for both channels [22]. We observe a similar increase in the noise measured over the full V_{EW} and V_{DC} range covered by the conductance maps shown in Fig. 1, see Supplemental Material [22]. Importantly, the precise calibration of the noise measurement setup [22] and of the injected current, along with the fact that for all \bar{G}_{QPC} , the thermal rounding of the noise is very well reproduced by a fixed temperature $T = 100 \text{ mK}$ equal to that of our fridge, precludes any error larger than 10 % in the extracted value of α [22]. The

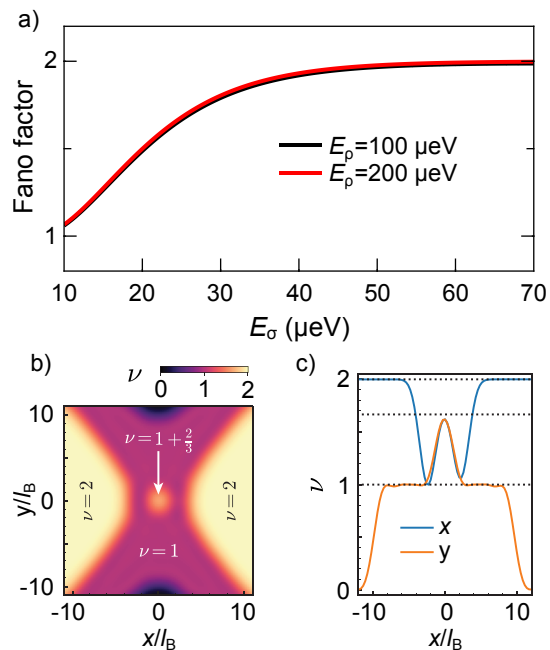


Figure 4. **(a)**, Calculated Fano factor of a $\nu = 2/3$ quantum dot versus dipole mode energy E_σ in the plasmon model, for two values of the charge mode energy E_ρ . **(b)**, Thomas-Fermi calculation of the filling factor variation at the QPC saddle point. x corresponds to the W-E direction, y to the S-N direction, and $x = y = 0$ to the center of the saddle point. **(c)**, Linecuts of the data of **(b)** in the x direction at $y = 0$ (blue) and in the y direction at $x = 0$ (orange). The horizontal dashed lines denote $\nu = 1$, $1 + 2/3$, and 2.

measured noise is thus significantly larger than expected, over the whole range of QPC transmission. We attribute this enhancement to the presence of the quantum dot at the QPC saddle point. Quantum dot physics can lead to non-Markovian charge transport [23], where the transfer of one charge across the quantum dot influences that of a subsequent charge. This yields super-Poissonian current fluctuations, that is, shot noise with effective Fano factors larger than 1. This has been extensively studied [23–35], including by some of our coauthors [36]; however, most of those mechanisms correspond to high-bias transport, where the quantum dot is either in the sequential tunneling regime, or in the inelastic cotunneling regime. Our data is obtained at energies below the inelastic cotunneling threshold (see Fig. 1b and c); in this regime, Fano factor enhancements can be observed in quantum dots inside which at least two edge channels circulate [37]. The noise enhancement mechanism, recently proposed in ref. [38], relies on strong electrostatic interactions between the two edge channels. These lead to two plasmonic eigenstates shared by both edge channels [39–47]: a fast, high-energy charge mode, and a slow, low-energy dipolar mode, called neutral mode, or spin mode. If the bias is comparable to the energy of the neutral mode, two competing tunneling processes come into

play: i) in the first the tunnelings of two subsequent electrons are independent and leave the state of the quantum dot unaffected, while ii) in the second an electron enters the quantum dot then exits leaving behind an excited neutral plasmonic mode within the dot. If the lifetime of this excitation is long enough, it can then be absorbed by the next tunneling charge, largely enhancing its tunneling probability [48–50]. This induces correlations in the tunneling events, and increases the noise to effective Fano factors up to 2 [38]. Fig. 3 shows a comparison of our results with a semiclassical realization of this process that ignores the microscopics of the quantum dot, in particular its edge channel structure. In this model (thick lines in Fig. 3), the tunneling correlations are simplified to the extreme case: when a charge goes through the dot with a probability p_t , the next one goes through the dot with a probability 1. After this second charge tunneling, the process is reset. The evolution of the Fano factor with the probability p_t can then be understood in the following way. For low p_t (corresponding to large τ_1 or low τ_2), the train of charges arriving on the dot generates individual kinks of transmitted charge $2e$, leading to a Fano factor close to 2. Inversely, for p_t close to 1 ($\tau_1 \rightarrow 0$ or $\tau_2 \rightarrow 1$), our model leads to individual kinks of charge e in the backscattered current and hence a Fano factor close to 1. The agreement between the experimental data and this model, without any fit parameters, is very reasonable in the range $0.5e^2/h < G_{\text{QPC}} < 1.5e^2/h$ (full lines), corresponding to $p_t < 0.5$. For larger p_t , sizeable deviations appear (dashed lines), and the calculated Fano factor reaches 1 for $G_{\text{QPC}} \rightarrow 0$. This is due to the fact that in our experiment, unity transmission across the dot correspond to resonant tunneling rather than transparent barriers. Note that this model relies on a large number of independent computations for each value of p_t ; the fluctuations shown in Fig. 3 correspond to a finite number of such computations.

According to the above discussion, the quantum dot requires two circulating edge channels for charge tunneling correlations to appear. Our conductance measurements show that the local filling factor at the QPC saddle point is at least 1 (purple region in Fig. 1d and e), and increases to give rise to the quantum dot. In order to accommodate two integer edge channels, the filling factor in the dot should reach $\nu = 3$, which is unlikely because of the very large cyclotron gap between the zeroth and first Landau levels of graphene. Thus, the filling factor in the dot is likely non-integer, potentially giving rise to fractional quantum Hall edge channels circulating in the dot. A good candidate is a local $\nu = 1 + 2/3$ state, which, in absence of disorder, hosts two counter-propagating edge states on top of an inert background at $\nu = 1$: a downstream integer one, and an upstream fractional one with conductance $1/3 \times e^2/h$ [51]. We have adapted the plasmon model of ref. [38] to the $\nu = 2/3$ case of counterpropagating channels with conductances

$1 \times e^2/h$ and $-1/3 \times e^2/h$ (see Supplemental Material [22]) to calculate the Fano factor through the quantum dot in the regime of small dot transmissions. The two main parameters of the model are the energies of the charge and dipole plasmon modes, respectively E_ρ and E_σ . Setting $T = 100$ mK and $V_{\text{DC}} = 50 \mu\text{V}$, we plot in Fig. 4 the evolution of the Fano factor versus E_σ for two values of E_ρ . As soon as E_σ is sizeably larger than the thermal energy, irrespective of the value of E_ρ , the Fano factor exceeds 1 and increases with E_σ until it saturates to 2, qualitatively matching our observations. We have validated our hypothesis of the local $\nu = 1 + 2/3$ state by performing Thomas-Fermi calculations of the filling factor at the QPC saddle point [22], (see Fig. 4b and c). In a previous work realized on the same device [20], this method had already shown that it was possible to generate a fractional island at the QPC saddle point. With electrostatic parameters (gate voltages, and hBN thickness) matching that of our experiment, we show that the filling factor at the QPC indeed increases from a local $\nu = 1$ background to a small zone at $\nu = 1 + 2/3$ at the center of the saddle point. Importantly, for the noise enhancement to occur in both outer and inner channels of bulk $\nu = 2$, the two channels circulating in the quantum dot require spin polarizations matching that of each edge channels of $\nu = 2$. The $\nu = 2/3$ state in graphene has been shown to be fully spin polarized at large magnetic fields [52]. Near the QPC, the $\nu = 2$ edge is defined by the $\nu = 0$ region below the N and S gates, leading to a canting of the spin polarizations of both edge channels with respect to the magnetic field [53]. This canting can thus reduce the energy cost for charges from either edge channel to tunnel into the spin-polarized quantum dot.

In conclusion, we have shown that self-reconstructed quantum dots at the saddle point of graphene QPCs can lead to a substantial increase in the shot noise. This increase, which we attribute to correlated charge tunneling across the dot mediated by electrostatically coupled counter-propagating QH edge channels circulating in the dot, can be detrimental to future experiments based on shot noise generated at a graphene QPC to probe the unique properties of edge excitations in the QH regime.

This work was funded by the ERC (ERC-2018-STG *QUAHQ*), by the “Investissements d’Avenir” LabEx PALM (ANR-10-LABX-0039-PALM), and by the Region Ile de France through the DIM QUANTIP. O.M. acknowledges funding from the ANR (ANR-23-CE47-0002 CRAQUANT). J.F. acknowledges support from the UC Berkeley College of Engineering Jane Lewis Fellowship. K.W. and T.T. acknowledge support from the JSPS KAKENHI (Grant Numbers 21H05233 and 23H02052), the CREST (JPMJCR24A5), JST and World Premier International Research Center Initiative (WPI), MEXT, Japan. M.S. acknowledges the support from the project PRIN2022 2022-PH852L(PE3) TopoFlags- “Non reciprocal supercurrent and topological transition in hybrid

Nb-InSb nanoflags” funded by the European community Next Generation EU within the programme “PNRR Missione Componente Investimento Fondo per il Programma Nazionale di Ricerca e Progetti di Rilevante Interesse Nazionale (PRIN)”. The authors warmly thank C. Altimiras and A. Assouline for enlightening discussions.

* Equal contribution.

† Equal contribution. Contact: olivier.maiellet@cea.fr

‡ Contact: preden.roulleau@cea.fr

§ Contact: francois.parmenier@phys.ens.fr

- [1] A. Kumar, L. Saminadayar, D. C. Glattli, Y. Jin, and B. Etienne, Experimental test of the quantum shot noise reduction theory, *Physical Review Letters* **76**, 2778 (1996).
- [2] L. Saminadayar, D. C. Glattli, Y. Jin, and B. Etienne, Observation of the $e/3$ fractionally charged Laughlin quasiparticle, *Physical Review Letters* **79**, 2526 (1997).
- [3] R. de Picciotto, M. Reznikov, M. Heiblum, V. Umansky, G. Bunin, and D. Mahalu, Direct observation of a fractional charge, *Nature* **389**, 162 (1997).
- [4] M. Reznikov, R. de Picciotto, T. G. Griffiths, M. Heiblum, and V. Umansky, Observation of quasiparticles with one-fifth of an electron’s charge, *Nature* **399**, 238 (1999).
- [5] M. Dolev, M. Heiblum, V. Umansky, A. Stern, and D. Mahalu, Observation of a quarter of an electron charge at the $\nu = 5/2$ quantum hall state, *Nature* **452**, 829 (2008).
- [6] H. Bartolomei, M. Kumar, R. Bisognin, A. Marguerite, J.-M. Berroir, E. Bocquillon, B. Plaçais, A. Cavanna, Q. Dong, U. Gennser, Y. Jin, and G. Fève, Fractional statistics in anyon collisions, *Science* **368**, 173 (2020).
- [7] J. Nakamura, S. Liang, G. C. Gardner, and M. J. Manfra, Direct observation of anyonic braiding statistics, *Nature Physics* **16**, 931 (2020).
- [8] A. Veillon, C. Piquard, P. Glidic, Y. Sato, A. Aassime, A. Cavanna, Y. Jin, U. Gennser, A. Anthore, and F. Pierre, Observation of the scaling dimension of fractional quantum hall anyons, *Nature* **632**, 517 (2024).
- [9] M. Ruelle, E. Frigerio, E. Baudin, J.-M. Berroir, B. Plaçais, B. Grémaud, T. Jonckheere, T. Martin, J. Rech, A. Cavanna, U. Gennser, Y. Jin, G. Ménard, and G. Fève, Time-domain braiding of anyons, [arXiv:2409.08685](https://arxiv.org/abs/2409.08685) (2024).
- [10] C. R. Dean, A. F. Young, P. Cadden-Zimansky, L. Wang, H. Ren, K. Watanabe, T. Taniguchi, P. Kim, J. Hone, and K. L. Shepard, Multicomponent fractional quantum hall effect in graphene, *Nature Physics* **7**, 693 (2011).
- [11] J. I. A. Li, C. Tan, S. Chen, Y. Zeng, T. Taniguchi, K. Watanabe, J. Hone, and C. R. Dean, Even-denominator fractional quantum hall states in bilayer graphene., *Science (New York, N.Y.)* **358**, 648 (2017).
- [12] A. A. Zibrov, C. Kometter, H. Zhou, E. M. Spanton, T. Taniguchi, K. Watanabe, M. P. Zaletel, and A. F. Young, Tunable interacting composite fermion phases in a half-filled bilayer-graphene Landau level, *Nature* **549**, 360 (2017).
- [13] C. Déprez, L. Veyrat, H. Vignaud, G. Nayak, K. Watanabe, T. Taniguchi, F. Gay, H. Sellier, and B. Sacépé,

- A tunable fabry–pérot quantum hall interferometer in graphene, *Nature Nanotechnology* **16**, 555 (2021).
- [14] Y. Ronen, T. Werkmeister, D. H. Najafabadi, A. T. Pierce, L. E. Anderson, Y. J. Shin, S. Y. Lee, Y. H. Lee, B. Johnson, K. Watanabe, T. Taniguchi, A. Yacoby, and P. Kim, Aharonov–bohm effect in graphene-based fabry–pérot quantum hall interferometers, *Nature Nanotechnology* **16**, 563 (2021).
- [15] T. Werkmeister, J. R. Ehrets, M. E. Wesson, D. H. Najafabadi, K. Watanabe, T. Taniguchi, B. I. Halperin, A. Yacoby, and P. Kim, Anyon braiding and telegraph noise in a graphene interferometer, [arXiv:2403.18983](https://arxiv.org/abs/2403.18983) (2024).
- [16] N. L. Samuelson, L. A. Cohen, W. Wang, S. Blanch, T. Taniguchi, K. Watanabe, M. P. Zaletel, and A. F. Young, Anyonic statistics and slow quasiparticle dynamics in a graphene fractional quantum hall interferometer, [arXiv:2403.19628](https://arxiv.org/abs/2403.19628) (2024).
- [17] J. H. Davies and I. A. Larkin, Theory of potential modulation in lateral surface superlattices, *Physical Review B* **49**, 4800 (1994).
- [18] L. A. Cohen, N. L. Samuelson, T. Wang, K. Klocke, C. C. Reeves, T. Taniguchi, K. Watanabe, S. Vijay, M. P. Zaletel, and A. F. Young, Nanoscale electrostatic control in ultraclean van der waals heterostructures by local anodic oxidation of graphite gates, *Nature Physics* **19**, 1502 (2023).
- [19] L. A. Cohen, N. L. Samuelson, T. Wang, T. Taniguchi, K. Watanabe, M. P. Zaletel, and A. F. Young, Universal chiral luttinger liquid behavior in a graphene fractional quantum hall point contact, *Science* **382**, 542 (2023).
- [20] L. A. Cohen, N. L. Samuelson, T. Wang, K. Klocke, C. C. Reeves, T. Taniguchi, K. Watanabe, S. Vijay, M. P. Zaletel, and A. F. Young, Spontaneous Localization at a Potential Saddle Point from Edge State Reconstruction in a Quantum Hall Point Contact, *Phys. Rev. Lett.* **134**, 076302 (2025).
- [21] Y. Blanter and M. Büttiker, Shot noise in mesoscopic conductors, *Physics Reports* **336**, 1 (2000).
- [22] See supplemental materials.
- [23] E. V. Sukhorukov, G. Burkard, and D. Loss, Noise of a quantum dot system in the cotunneling regime, *Physical Review B* **63**, 125315 (2001).
- [24] W. Belzig, Full counting statistics of super-poissonian shot noise in multilevel quantum dots, *Physical Review B* **71**, 161301 (2005).
- [25] A. Thielmann, M. H. Hettler, J. König, and G. Schön, Cotunneling current and shot noise in quantum dots, *Physical Review Letters* **95**, 146806 (2005).
- [26] E. Onac, F. Balestro, B. Trauzettel, C. F. J. Lodewijk, and L. P. Kouwenhoven, Shot-noise detection in a carbon nanotube quantum dot, *Physical Review Letters* **96**, 026803 (2006).
- [27] I. Weymann, J. Barnaś, and S. Krompiewski, Theory of shot noise in single-walled metallic carbon nanotubes weakly coupled to nonmagnetic and ferromagnetic leads, *Physical Review B* **76**, 155408 (2007).
- [28] J. Aghassi, M. H. Hettler, and G. Schön, Cotunneling assisted sequential tunneling in multilevel quantum dots, *Applied Physics Letters* **92**, 202101 (2008).
- [29] A. Carmi and Y. Oreg, Enhanced shot noise in asymmetric interacting two-level systems, *Physical Review B* **85**, 045325 (2012).
- [30] K. Kaasbjerg and W. Belzig, Full counting statistics and shot noise of cotunneling in quantum dots and single-molecule transistors, *Physical Review B* **91**, 235413 (2015).
- [31] Y. Zhang, L. DiCarlo, D. T. McClure, M. Yamamoto, S. Tarucha, C. M. Marcus, M. P. Hanson, and A. C. Gosard, Noise correlations in a coulomb-blockaded quantum dot, *Physical Review Letters* **99**, 036603 (2007).
- [32] O. Zarchin, Y. C. Chung, M. Heiblum, D. Rohrlich, and V. Umansky, Electron bunching in transport through quantum dots in a high magnetic field, *Physical Review Letters* **98**, 066801 (2007).
- [33] C. Fricke, F. Hohls, W. Wegscheider, and R. J. Haug, Bimodal counting statistics in single-electron tunneling through a quantum dot, *Physical Review B* **76**, 155307 (2007).
- [34] Y. Okazaki, S. Sasaki, and K. Muraki, Shot noise spectroscopy on a semiconductor quantum dot in the elastic and inelastic cotunneling regimes, *Physical Review B* **87**, 041302 (2013).
- [35] M.-C. Harabula, V. Ranjan, R. Haller, G. Fülöp, and C. Schönberger, Blocking-state influence on shot noise and conductance in quantum dots, *Physical Review B* **97**, 115403 (2018).
- [36] M. Seo, P. Roulleau, P. Roche, D. Glattli, M. Sanquer, X. Jehl, L. Hutin, S. Barraud, and F. D. Parmentier, Strongly correlated charge transport in silicon metal-oxide-semiconductor field-effect transistor quantum dots, *Physical Review Letters* **121**, 027701 (2018).
- [37] H. Choi, I. Sivan, A. Rosenblatt, M. Heiblum, V. Umansky, and D. Mahalu, Robust electron pairing in the integer quantum hall effect regime, *Nature Communications* **6**, 7435 (2015).
- [38] G. A. Frigeri and B. Rosenow, Electron pairing in the quantum hall regime due to neutralon exchange, *Physical Review Research* **2**, 043396 (2020).
- [39] C. L. Kane, M. P. A. Fisher, and J. Polchinski, Randomness at the edge: Theory of quantum hall transport at filling $\nu = 2/3$, *Physical Review Letters* **72**, 4129 (1994).
- [40] C. L. Kane and M. P. A. Fisher, Impurity scattering and transport of fractional quantum hall edge states, *Physical Review B* **51**, 13449 (1995).
- [41] X.-G. Wen, Topological orders and edge excitations in fractional quantum hall states, *Advances in Physics* **44**, 405 (1995).
- [42] E. Sukhorukov and V. Cheianov, Resonant dephasing in the electronic mach-zehnder interferometer, *Physical Review Letters* **99**, 156801 (2007).
- [43] I. Levkivskiy and E. Sukhorukov, Dephasing in the electronic mach-zehnder interferometer at filling factor $\nu = 2$, *Physical Review B* **78**, 045322 (2008).
- [44] D. Ferraro, A. Braggio, N. Magnoli, and M. Sassetti, Neutral modes’ edge state dynamics through quantum point contacts, *New Journal of Physics* **12**, 013012 (2010).
- [45] M. Carrega, D. Ferraro, A. Braggio, N. Magnoli, and M. Sassetti, Spectral noise for edge states at the filling factor $\nu = 5/2$, *New Journal of Physics* **14**, 023017 (2012).
- [46] E. Bocquillon, V. Freulon, J.-M. Berroir, P. Degiovanni, B. Plaçais, A. Cavanna, Y. Jin, and G. Fève, Separation of neutral and charge modes in one-dimensional chiral edge channels., *Nature Communications* **4**, 1839 (2013).
- [47] R. H. Rodriguez, F. D. Parmentier, D. Ferraro, P. Roulleau, U. Gennser, A. Cavanna, M. Sassetti, F. Portier, D. Mailly, and P. Roche, Relaxation and revival of quasiparticles injected in an interacting quantum hall liquid,

- [Nature Communications](#) **11**, 2426 (2020).
- [48] F. Cavaliere, A. Braggio, M. Sassetti, and B. Kramer, Spin effects in transport through non-fermi-liquid quantum dots, [Physical Review B](#) **70**, 125323 (2004).
- [49] J. U. Kim, J. M. Kinaret, and M.-S. Choi, Shot noise enhancement from non-equilibrium plasmons in luttinger liquid junctions, [Journal of Physics: Condensed Matter](#) **17**, 3815 (2005).
- [50] J. U. Kim, M.-S. Choi, I. V. Krive, and J. M. Kinaret, Nonequilibrium plasmons and transport properties of a double-junction quantum wire, [Low Temperature Physics](#) **32**, 1158 (2006).
- [51] A. H. MacDonald, Edge states in the fractional-quantum-hall-effect regime, [Physical Review Letters](#) **64**, 220 (1990).
- [52] Y. Zeng, J. Li, S. Dietrich, O. Ghosh, K. Watanabe, T. Taniguchi, J. Hone, and C. Dean, High-quality magnetotransport in graphene using the edge-free corbino geometry, [Physical Review Letters](#) **122**, 137701 (2019).
- [53] S. Takei, A. Yacoby, B. I. Halperin, and Y. Tserkovnyak, Spin superfluidity in the $\nu = 0$ quantum hall state of graphene, [Physical Review Letters](#) **116**, 216801 (2016).

Supplemental Material for "Enhanced shot noise in graphene quantum point contacts with electrostatic reconstruction"

M. Garg,^{1,2,*} O. Maillet,^{1,†} N. L. Samuelson,³ T. Wang,^{4,5} J. Feng,⁶ L. A. Cohen,³ K. Watanabe,⁷ T. Taniguchi,⁸ P. Roulleau,^{1,‡} M. Sassetti,^{9,10} M. Zaletel,^{4,5} A. F. Young,³ D. Ferraro,^{9,10} P. Roche,¹ and F.D. Parmentier^{1,11,§}

¹ *Université Paris-Saclay, CEA, CNRS, SPEC, 91191 Gif-sur-Yvette cedex, France*

² *Department of Physics, Indian Institute of Technology Roorkee, Uttarakhand 247667, India*

³ *Department of Physics, University of California at Santa Barbara, Santa Barbara CA 93106, USA*

⁴ *Department of Physics, University of California at Berkeley, Berkeley, CA 94720, USA*

⁵ *Material Science Division, Lawrence Berkeley National Laboratory, Berkeley, CA 94720, USA*

⁶ *Graduate Group in Applied Science & Technology, University of California, Berkeley, California 94720, USA*

⁷ *Research Center for Electronic and Optical Materials, National Institute for Materials Science, 1-1 Namiki, Tsukuba 305-0044, Japan*

⁸ *Research Center for Materials Nanoarchitectonics, National Institute for Materials Science, 1-1 Namiki, Tsukuba 305-0044, Japan*

⁹ *Dipartimento di Fisica, Università di Genova, Via Dodecaneso 33, 16146, Genova, Italy*

¹⁰ *SPIN-CNR, Via Dodecaneso 33, 16146, Genova, Italy*

¹¹ *Laboratoire de Physique de l'École normale supérieure, ENS, Université PSL, CNRS, Sorbonne Université, Université Paris Cité, F-75005 Paris, France*

(Dated: March 24, 2025)

SAMPLE FABRICATION

The graphite top gate was patterned via AFM anodic oxidation lithography (as outlined in ref. [1], a prior study of the same device, which gives more detailed fabrication process parameters). Then, the van der Waals heterostructure was stacked via a dry transfer process using a polycarbonate film on a dome shaped PDMS to pick up each successive layer. The stack was deposited onto a doped silicon substrate with a 285nm-thick thermally-grown oxide layer. 30kV e-beam lithography was then used to define the pattern of an e-beam evaporated 40nm aluminum hard mask, and the device outline was etched via an inductively-coupled CHF₃/O₂ plasma etch. The aluminum mask was removed with a dilute solution of TMAH, and a PMMA mask written via a second EBL step before e-beam evaporation of Cr/Pd/Au (3/15/185 nm) edge contacts. Finally, another PMMA mask was used to define narrow trenches which were etched into each contact via an additional CHF₃/O₂ plasma etch step.

MEASUREMENT SETUP

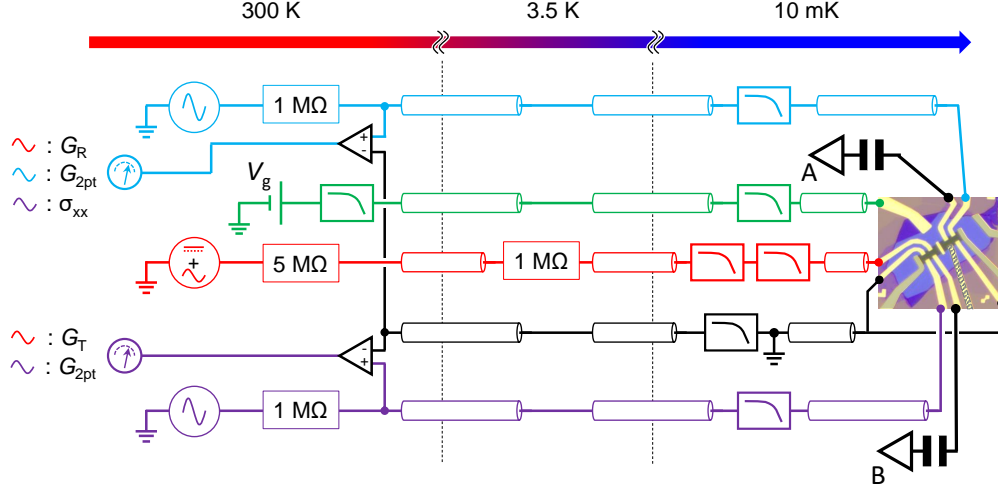
Conductance measurements

A detailed description of the conductance measurements is shown in Supplemental Fig. 1. The measurements were performed using lock-in techniques at low frequency, below 10 Hz. All lines, including current feed (red in Supplemental Fig. 1) and back gate (green in Supplemental Fig. 1) are heavily filtered at the mixing chamber stage of our dilution refrigerator using cascaded *RC* filters. The effect of those filters (both in terms of series resistance and capacitive cutoff) are taken into account in our data. All measurements are performed using differential amplifiers (CELIANS EPC-1B) referenced to the cold ground (black in Fig. 1) The latter is directly connected (both electrically and thermally) to the mixing chamber stage. The current feed line includes a 1 M Ω series bias resistor thermally anchored to the 3.5 K stage of our dilution refrigerator.

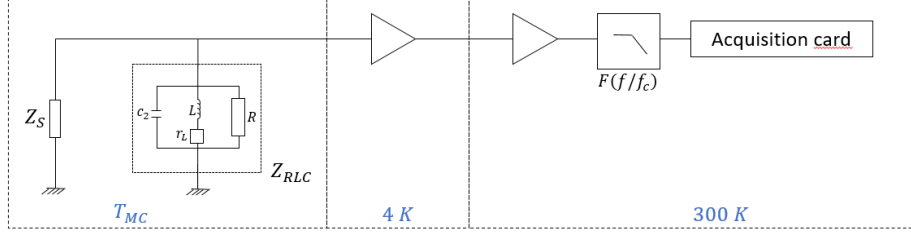
Noise measurements: setup and calibration

The noise which is measured is the following one :

$$S_{th,v}^{meas} = G^2 \times \int_{\Delta f} df F\left(\frac{f}{f_c}\right) \left[S_{v,amp}^2 + |Z_{||}|^2 \left(S_{i,amp}^2 + 4k_B T Re\left(\frac{1}{Z_{RLC}}\right) + S_{i,sample}^2 \right) \right] \quad (1)$$



Supplemental Figure 1: Layout of the wiring for the conductance measurements. Lines are color-coded (blue: T-side conductance; green: back gate; red: dc current feed; purple: R-side conductance; black: cold ground).



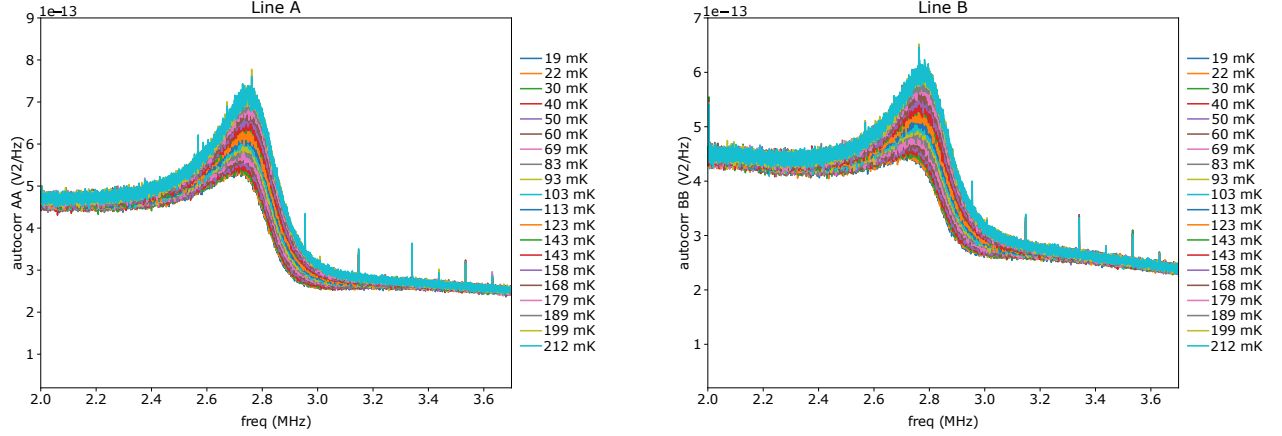
Supplemental Figure 2: Noise measurement circuit from the sample to the acquisition card. The resonator is made with a capacitor c_2 , an inductor L with an effective resistance r_L and a resistance R which represents the losses on the circuit.

Where G is the overall gain of the amplification chain, $F(f/f_c)$ a second order low-pass filter function corresponding to the antialiasing filters (see Supplemental Fig. 2), $S_{i,amp}^2$ and $S_{v,amp}^2$ are the current and voltage noise of the amplifier, $4k_B T Re(\frac{1}{Z_{RLC}})$ the thermal noise of the LRC circuit resonator, $Z_{||}$ the parallel impedance of the LRC circuit resonator and the sample, Δf the integration bandwidth, and $S_{i,sample}^2$ the current noise of the sample, which includes its thermal noise. We determine these parameter with a temperature calibration where we measured the equilibrium noise for temperature ranging between 10 and 200 mK, for various filling factors. Supplemental Fig. 3 shows typical raw spectra obtained from this calibration. We first remove the contribution of the temperature-independent terms by calculating the difference between each spectrum and the average of all spectra:

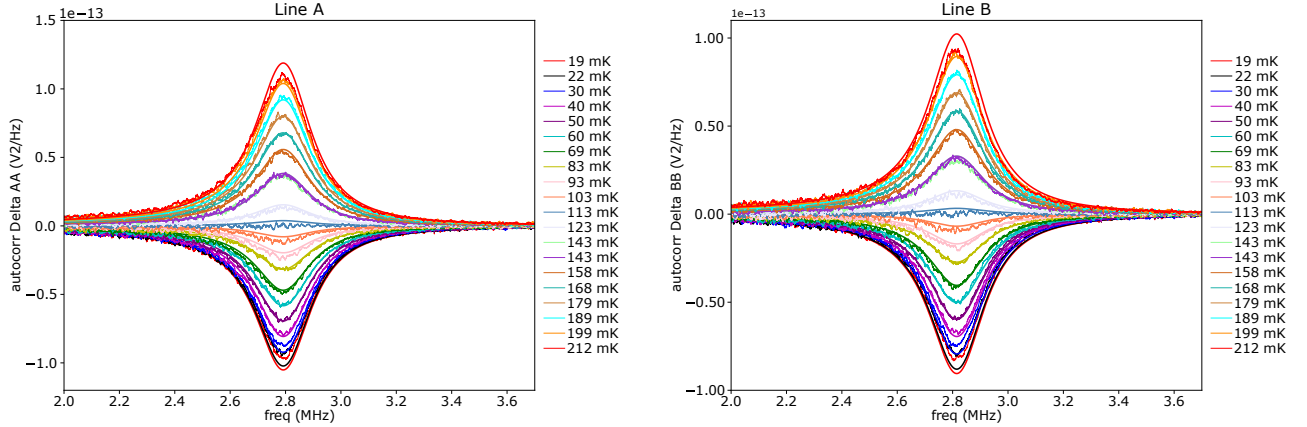
$$\Delta S_v = S_{th}^{meas} - \langle S_{th}^{meas} \rangle_T, \quad (2)$$

yielding the curves shown in Supplemental Fig. 4, given by the following equation, assuming that the temperature of the resonator and of the sample are equal:

$$\Delta S_v^{meas} = G^2 \int_{\Delta f} F\left(\frac{f}{f_c}\right) 4k_B \Delta T |Z_{||}|^2 \left[\text{Re}\left(\frac{1}{Z_{RLC}}\right) + \nu \times e^2/h \right] \quad (3)$$



Supplemental Figure 3: Raw noise spectra for line A (left) and B (right) for different temperatures ranging from 19 mK to 212 mK. Data taken at $\nu_{EW} = 2$, at $B = 13$ T.



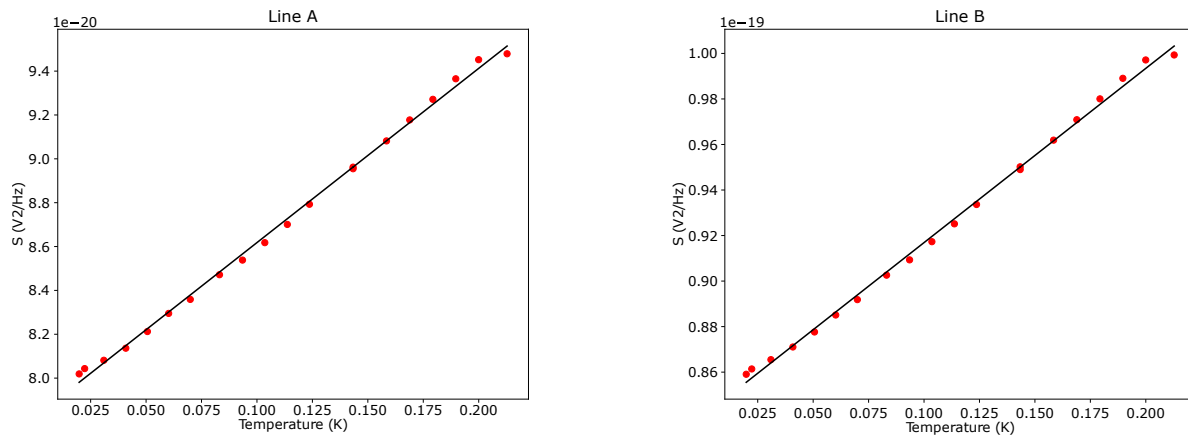
Supplemental Figure 4: Differential noise spectra for line A (left) and B (right), corresponding to the raw spectra shown in Supplemental Fig. 3. The smooth lines are fits using Supplemental Eq. 3

The parameters of the LCR circuit are found by fitting the equation 3 from the measured noise for a fixed value of ν . The voltage noise of the amplifier can be found from the intercept in temperature dependence of the integrated noise, as shown in Supplemental Fig. 5.

This calibration can be applied to the measurement, to analyze the current noise of the sample. The calibrated noise is the following :

$$\Delta S = \frac{\Delta f \Delta S_v^{meas}}{G^2 \int_{\Delta f} df F\left(\frac{f}{f_c}\right) |Z_{||}|^2} \quad (4)$$

Three separate calibration runs were performed over a course of two months during which the sample was measured. For each run, we have performed the calibration at bulk filling factor $\nu_{EW} = 2$ and 3. The overall uncertainty on the value of the gain is about 6 %. Importantly, the extracted values are very similar, within the same uncertainty, to the values reported in previous noise measurements in graphene samples done in our group, focusing on the quantitative measurement of the quantized heat flow in QH edge channels [2,3]. Given this, the increased shot noise reported in the main text cannot be attributed to a measurement or calibration error.



Supplemental Figure 5: Integrated noise spectra from Supplemental Fig. 3 versus temperature. The line is a linear fit of the data.

	A 07/07/22	B 07/07/22	A 08/04/22	B 08/04/22	A 08/30/22	B 08/30/22
R	500 k Ω	400 k Ω	500 k Ω	400 k Ω	500 k Ω	400 k Ω
L	22 μ H	22 μ H	22 μ H	22 μ H	22 μ H	22 μ H
c_2	147.4 pF	144.8 pF	147.4 pF	144.8 pF	147.4 pF	144.8 pF
r_L	22 Ω	22 Ω	22 Ω	22 Ω	22 Ω	22 Ω
G	3475 \pm 75	3150 \pm 50	3550 \pm 50	3250 \pm 50	3550 \pm 50	3250 \pm 50

Supplemental Figure 6: Table of the calibration parameters obtained for both lines in three separate calibration runs over a period of two months.

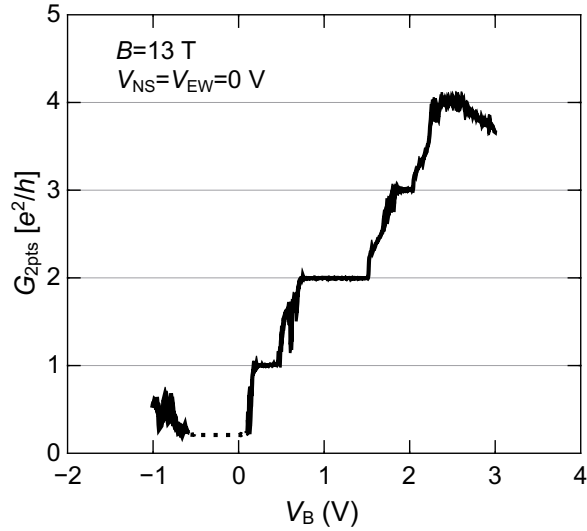
ADDITIONAL DATA AT $B = 13$ T

Conductance

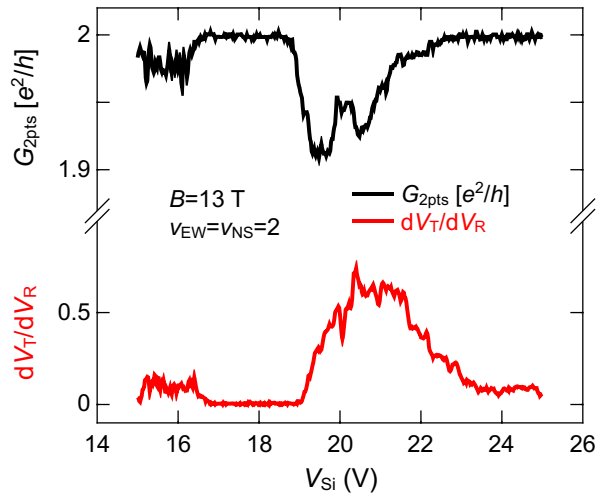
The QPC is operated at $B = 13$ T by tuning the EW regions to $\nu = 2$ using both back and EW gates. Supplemental Fig. 7 shows a 2 point measurement of the Hall conductance versus back gate voltage, displaying the plateaus for $\nu = 0, 1, 2, 3$ and 4. We set the value of the back gate voltage to the $\nu = 2$ plateau, then sweep the EW gate voltage to locate the range of the $\nu = 0$ plateau that will be used for the NS QPC gate. Having fixed both the back gate and the NS gate, we sweep the EW gate along the $\nu = 2$ plateau to obtain the conductance data shown in main text Fig. 1.

In addition to the graphite gate, the silicon back gate is used to locally dope the graphene flake close to its metallic edge contacts. The voltage applied to the silicon gate is selected by measuring the variation of the transconductance signal dV_T/dV_R , which reflects the quality of the grounded contact downstream of contact R. Supplemental Fig. 8 shows the result for $\nu_{EW} = \nu_{NS} = 2$, at $B = 13$ T: around $V_{Si} = 18$ V, the signal vanishes, signaling an optimal transmission to the grounded contact. In the results shown in the main text we have thus set $V_{Si} = 18$ V.

The dc current transmitted across the QPC I_T is obtained by measuring the differential transmission dI_T/dI_0 at finite dc current I_0 , which is then integrated. Supplemental Fig. 9 shows typical examples of this procedure, for several EW gate voltages. The average QPC conductance \bar{G}_{QPC} is directly obtained from the dI_T/dI_0 measurements.



Supplemental Figure 7: Hall conductance (measured in a 2 point configuration) of the sample versus back gate voltage, at $B = 13$ T and $T = 100$ mK, for $V_{EW} = V_{NS} = 0$ V. The dashed line region corresponds to $\nu = 0$, where the lock-in preamplifiers saturate.



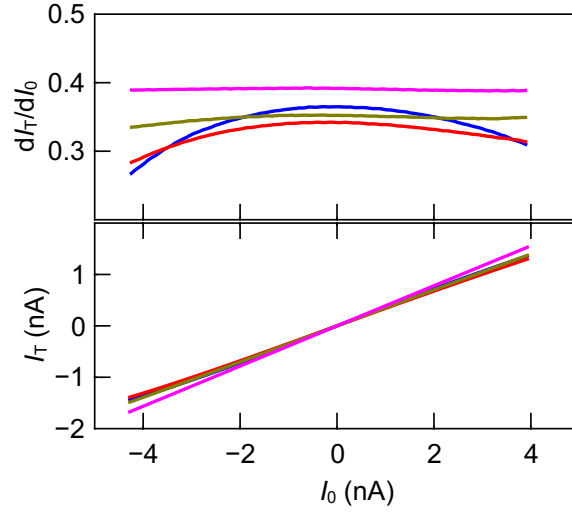
Supplemental Figure 8: Hall conductance (measured in a 2 point configuration - black) and transconductance dV_T/dV_R (red) versus silicon back gate voltage, for bulk filling factors $\nu_{EW} = \nu_{NS} = 2$, at $B = 13$ T.

Noise

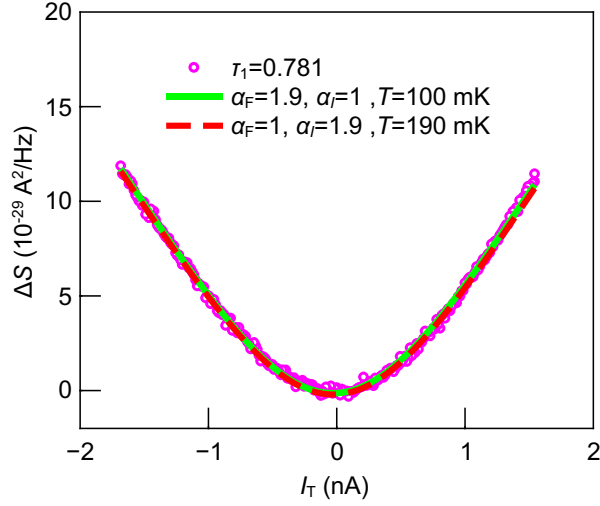
The noise measurements are fitted with main text Eq. 1, which expresses the noise as a function of the transmitted current I_T , with the I_T and \bar{G}_{QPC} obtained from conductance measurements (see above), the temperature fixed to $T = 100$ mK, and the Fano factor F as the only free parameter. Main text Eq. 1 has a slightly unusual expression, as the noise is more commonly expressed as a function of the dc voltage V_{dc} applied to the sample [4]:

$$\Delta S(V_{dc}) = \frac{2e^2}{h} \sum_i \tau_i (1 - \tau_i) \left(eV_{dc} \times \coth\left(\frac{eV_{dc}}{2k_B T}\right) - 2k_B T \right). \quad (5)$$

This equation can be expressed as a function of the transmitted current $I_T = \bar{G}_{QPC} V_{dc}$:



Supplemental Figure 9: Top: QPC transmission dI_T/dI_0 versus dc current I_0 , for different gate voltages corresponding to the transmission of the outer channel. Bottom: corresponding transmitted current I_T obtained by integration.



Supplemental Figure 10: Symbols: noise versus transmitted current, for $\tau_1 = 0.781$. Green continuous line: fit with the Fano factor prefactor α_F used as a fit parameters, with the temperature fixed to 100 mK and no prefactor on the transmitted current. Red dashed line: fit with a fixed $\alpha_F = 1$, and the temperature and the transmitted current prefactor used as fit parameters.

$$\Delta S(I_T) = \frac{2e^2}{h} \sum_i \tau_i (1 - \tau_i) \left(e^{-\frac{I_T}{\bar{G}_{\text{QPC}}}} \times \coth\left(\frac{eI_T}{2\bar{G}_{\text{QPC}}k_B T}\right) - 2k_B T \right). \quad (6)$$

The above equation thus already contains the $I_T \times \coth\left(\frac{eI_T}{2\bar{G}_{\text{QPC}}k_B T}\right)$ of main text Eq. 1, and can be further rewritten as:

$$\Delta S(I_T) = 2 \frac{e^2}{h} \frac{e}{\bar{G}_{\text{QPC}}} \sum_i \tau_i (1 - \tau_i) \left(I_T \times \coth\left(\frac{eI_T}{2\bar{G}_{\text{QPC}}k_B T}\right) - 2\bar{G}_{\text{QPC}} \frac{k_B T}{e} \right). \quad (7)$$

Recalling that $\bar{G}_{\text{QPC}} = \frac{e^2}{h} \sum_i \tau_i$, we obtain:

$$\Delta S(I_T) = 2e \frac{\sum_i \tau_i (1 - \tau_i)}{\sum_i \tau_i} \left(I_T \times \coth\left(\frac{eI_T}{2\bar{G}_{\text{QPC}} k_B T}\right) - 2\bar{G}_{\text{QPC}} \frac{k_B T}{e} \right). \quad (8)$$

Using the standard definition of the Fano factor [4] $F = \frac{\sum_i \tau_i (1 - \tau_i)}{\sum_i \tau_i}$, we finally obtain main text Eq. 1:

$$\Delta S(I_T) = 2eF \left(I_T \times \coth\left(\frac{eI_T}{2\bar{G}_{\text{QPC}} k_B T}\right) - 2\bar{G}_{\text{QPC}} \frac{k_B T}{e} \right), \quad (9)$$

Besides the calibration of the noise measurement setup, the calibration of the transmitted dc current can affect the values of the extracted Fano factors. If our results were due to an error on the dc current, this error would have to be more than 50 %. The line through which we apply the dc current I_0 is the same through which we apply the lock in excitation dI_0 (see Supplemental Fig. 1). The quantized values of the differential conductances measured at a few Hz that are shown in the main text attest that the calibration of this line is correct. To further discard this hypothesis, we have also fitted the noise versus I_T data shown in main text Fig. 2 with a modified version of main text Eq. 1, where a prefactor α_I in front of the transmitted current is used as a fit parameter instead of the prefactor α that use for the Fano factor (thus, α is fixed to 1). The only way to obtain reasonable fits is then to also let the temperature be a fit parameter, allowing to reproduce the thermal rounding at low bias. Supplemental Fig. 10 shows such a fit, along with that used in the main text: a good fit of the data can be obtain with $\alpha = 1$, at the cost of having a large $\alpha_I = 1.9$ as well as a large temperature $T = 190$ mK. This is doubly unlikely, as not only this would imply a large error on the current calibration, but also one on the electron temperature. From the calibration of the noise measurement, and also from previous experiments in the same fridge showing base electron temperatures as low as 11 mK [2], we know that the electron temperature in the sample closely follows that of our refrigerator above 50 mK.

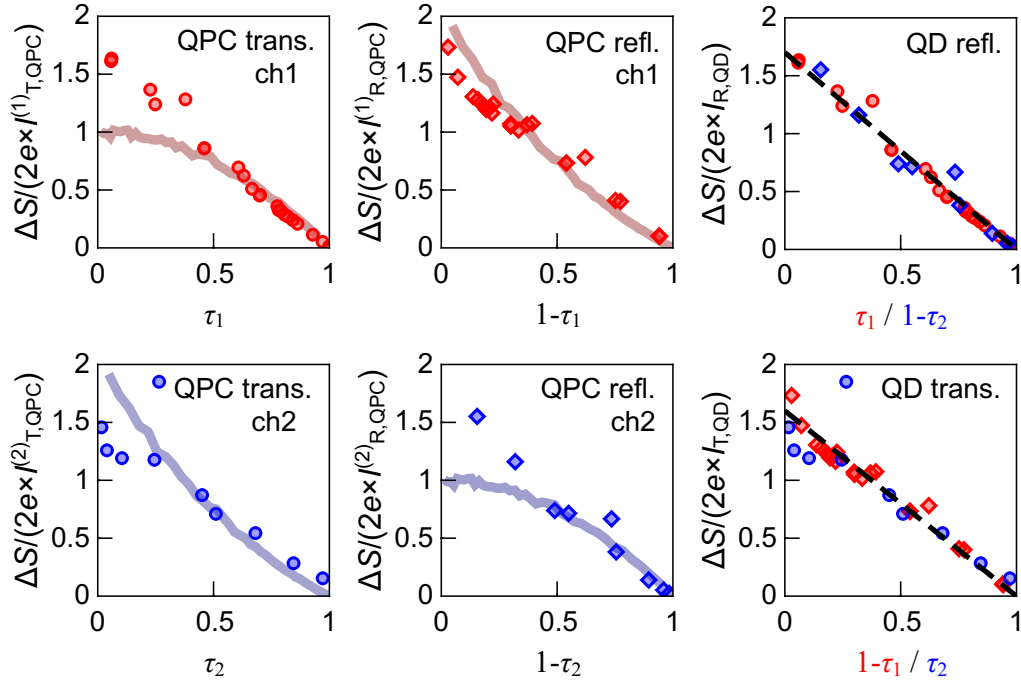
As plotted in main text Fig. 3a), the Fano factor corresponds to the ratio between the excess noise and the total current transmitted through the QPC. Plotting it as in main text Fig. 3a) versus conductance across the QPC thus corresponds to the usual plot for a QPC V versus $\sum \tau_i$, where τ_i is the transmission of the i -th channel across the QPC. There are however several other ways to plot the same noise data using different definition of the Fano factor: individual Fano factors for each channel, and Fano factor defined in reflection rather than in transmission. Recalling that I_0 is the total dc current flowing towards the QPC, with each channel carrying $I_0/2$, one can define the transmitted and reflected currents for each channel through the QPC and or the quantum dot:

$$\begin{aligned} I_{\text{T,QPC}}^{(1)} &= \tau_1 I_0/2 \\ I_{\text{R,QPC}}^{(1)} &= (1 - \tau_1) I_0/2 \\ I_{\text{T,QPC}}^{(2)} &= \tau_2 I_0/2 \\ I_{\text{R,QPC}}^{(2)} &= (1 - \tau_2) I_0/2 \\ I_{\text{T,QD}}^{(1)} &= (1 - \tau_1) I_0/2 = I_{\text{R,QPC}}^{(1)} \\ I_{\text{R,QD}}^{(1)} &= \tau_1 I_0/2 = I_{\text{T,QPC}}^{(1)} \\ I_{\text{T,QD}}^{(2)} &= \tau_2 I_0/2 = I_{\text{T,QPC}}^{(2)} \\ I_{\text{R,QD}}^{(2)} &= (1 - \tau_2) I_0/2 = I_{\text{R,QPC}}^{(2)} \end{aligned} \quad (10)$$

The inversion between the current transmitted through the QPC and through the quantum dot for the outer channel (channel $i = 1$) again stems from the fact that the quantum dot couples the outer edge channel from the west side to the east side in reflection (see main text). Thus, one can define 4 different channel-specific Fano factors:

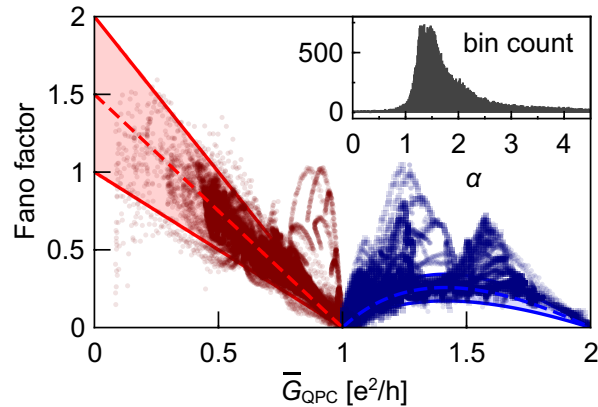
$$\begin{aligned}
F_{T,\text{QPC}}^{(1)} &= F_{R,\text{QD}}^{(1)} = \frac{\Delta S}{2eI_{T,\text{QPC}}^{(1)}} = \frac{\Delta S}{2eI_{R,\text{QD}}^{(1)}} = \frac{\Delta S}{2e\tau_1 I_0/2} \\
F_{R,\text{QPC}}^{(1)} &= F_{T,\text{QD}}^{(1)} = \frac{\Delta S}{2eI_{R,\text{QPC}}^{(1)}} = \frac{\Delta S}{2e(1-\tau_1)I_0/2} = F_{T,\text{QPC}}^{(1)} \times \frac{\tau_1}{(1-\tau_1)} \\
F_{T,\text{QPC}}^{(2)} &= F_{T,\text{QD}}^{(2)} = \frac{\Delta S}{2eI_{T,\text{QPC}}^{(2)}} = \frac{\Delta S}{2eI_{T,\text{QD}}^{(2)}} = \frac{\Delta S}{2e\tau_2 I_0/2} \\
F_{R,\text{QPC}}^{(2)} &= F_{R,\text{QD}}^{(2)} = \frac{\Delta S}{2eI_{R,\text{QPC}}^{(2)}} = \frac{\Delta S}{2e(1-\tau_2)I_0/2} = F_{T,\text{QPC}}^{(2)} \times \frac{\tau_2}{(1-\tau_2)}
\end{aligned}$$

(11)



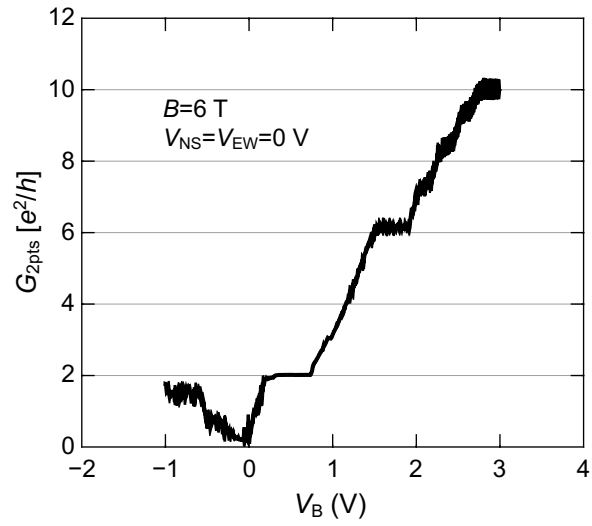
Supplemental Figure 11: Fano factor for each channel (red: outer, blue: inner), corresponding to the dataset of main text Fig. 3a), defined and plotted with respect to the QPC transmission (left column) and reflection (middle column). The thick line is the result of the simplified model for a single channel. Right column: Fano factor for each channel defined and plotted with respect to the quantum dot reflection (upper right panel) and transmission (lower right channel). The black dashed lines are linear functions.

Using the data shown in main text Fig. 3a), we define τ_1 and τ_2 from the measured \bar{G}_{QPC} , allowing to plot the four above-defined Fano factors versus their respective transmission/reflection. Supplementary Fig. 11 shows the corresponding plots, generalizing and confirming for all configurations the observation made in the main text. The Fano factor shows a linear decrease with transmission/reflection, with similar quantitative behaviors when plotting the Fano factor with respect to the quantum dot. The black dashed lines in the right panels are functions $\alpha(1-x)$, with a prefactor $\alpha = 1.7$ for the quantum dot reflection data (upper right panel), and $\alpha = 1.6$ for the quantum dot transmission data (lower right panel). We also plot the results of the simplified model (thick lines in the left and middle columns): when plotted in reflection with respect to the quantum dot (upper right and lower middle panels), the calculated Fano factor saturates to 1 at low quantum dot reflection, again showcasing the fact that since this model does not describe the internal dynamics of the dot, when most of the charges go through the quantum dot, rare reflection events can only involve a single charge.

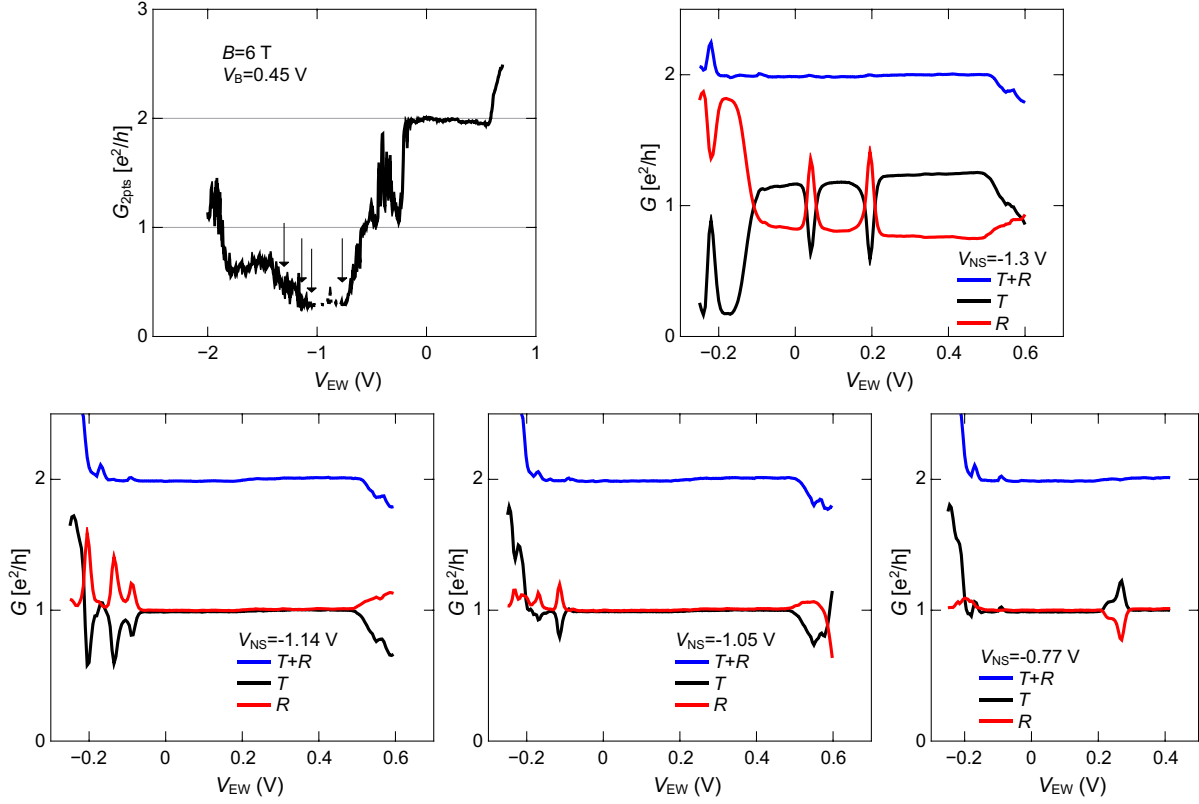


Supplemental Figure 12: Fano factor versus QPC conductance for the whole datasets corresponding to the two conductance maps shown in main text Fig. 1: red symbols for Fig. 1a), dark blue symbols for Fig. 1b). The red (resp. blue) shaded areas correspond to the Fano factor predictions with α between 1 and 2 (dashed line: $\alpha = 1.5$). Inset: bin count of the values of α extracted from the data in the main panel (bin size: 0.1).

The enhanced noise prefactor is also observed in the noise measured over the full V_g and V_{dc} range covered by the conductance maps shown in main text Fig. 1. We compute the Fano factor by dividing the measured noise by the expected Poisson noise $2e|I_T|$. The contribution of the thermal rounding is taken into account by adding to the excess noise ΔS a correction factor $4e^2/h\tau_{\{1,2\}}(1 - \tau_{\{1,2\}})k_B T$. The obtained values of the Fano factor are plotted in Fig. 12 as a function of \bar{G}_{QPC} , for all points appearing in the conductance maps except for those at $|V_{dc}| < 20 \mu V$. The data generally follows the Fano factor formula of main text Eq. 2, with clear shot noise suppression for integer \bar{G}_{QPC} . However, the corresponding values of α are clearly larger than 1, with a majority of points lying in between $\alpha = 1$ and 2 (red and blue shaded areas). The inset of Supplemental Fig. 12 shows the distribution of the extracted α over all measured data (approx. 72000 points), with a very pronounced peak at $\alpha \approx 1.5$. The distribution is clearly skewed towards large values of α , with a very small minority of data corresponding to $\alpha = 1$.

ADDITIONAL DATA AT $B = 6$ T

Supplemental Figure 13: Hall conductance (measured in a 2 point configuration) of the sample versus back gate voltage, at $B = 6$ T and $T = 300$ mK, for $V_{EW} = V_{NS} = 0$.



Supplemental Figure 14: Upper left: Hall conductance (measured in a 2 point configuration) of the sample versus V_{EW} , at $B = 6$ T, $T = 300$ mK, and for $V_B = 0.45$ V. Upper right, and lower panels: differential conductances (similar to main text Fig. 2a: blue (resp. red): transmitted (resp. reflected) conductance. Green: sum of the transmitted and reflected conductances) versus V_{EW} , for various values of V_{NS} indicated by the arrows in the upper left panel, corresponding to $\nu_{NS} \approx 0$.

**PLASMON MODEL FOR THE ENHANCEMENT OF THE FANO FACTOR THROUGH TUNNELING
ACROSS A QUANTUM HALL ISLAND AT $\nu = 2/3$**

Model

We consider two integer quantum Hall channels at filling factor $\nu = 1(+1)$ (where the additional $\nu = 1$ channel in parenthesis can be seen as an inert plateau not involved in the dynamics) playing the role of leads and coupled by means of a fractional quantum Hall dot at $\nu = 2/3(+1)$ (emerging again on top of the same inert integer plateau). The electron tunneling between these leads (indicated in the following as right R and left L respectively) and the dot will be considered as local.

In the following we will discuss the Hamiltonian contributions describing the various parts of this system.

Hamiltonians of the leads

The leads are described by the Hamiltonians (from now on we will consider $\hbar = 1$)

$$\hat{H}_{R/L} = \mp iv \int_0^{+\infty} dx \hat{\Psi}_{R/L}^\dagger(x) \partial_x \hat{\Psi}_{R/L}(x) \quad (12)$$

with $\hat{\Psi}_{R/L}(x)$ the annihilation field operators for an electron in the R and L reservoir respectively. In the above Equation we have considered, without loss of generality, the fact that the two leads can be described in terms of one-dimensional chiral free fermions propagating with velocity v along semi-infinite edge channels. According to this, the reservoirs at fixed temperature T and voltages $V_{L/R}$ can be described in terms of the Fermi distributions

$$f_{L/R}(E) = \frac{1}{1 + \exp[(E - eV_{L/R})/k_B T]} \quad (13)$$

where e is the electron charge and k_B is the Boltzmann constant.

In order to drive the system out of equilibrium and induce a current across the dot, a constant voltage bias

$$V = V_L - V_R \quad (14)$$

is applied between the reservoirs. For sake of simplicity we will assume the voltage drops as symmetric.

Hamiltonian of the dot

Recalling the conventional picture for the edge channels of a quantum Hall state at $\nu = 2/3$, the Hamiltonian of a quantum dot of circumference L can be written as [5–8]

$$\begin{aligned} \hat{H}_D = & \frac{1}{4\pi} \int_0^L dx \left[v_1 (\partial_x \hat{\phi}_1)^2 + 3v_2 (\partial_x \hat{\phi}_2)^2 + 2v_{12} \partial \hat{\phi}_1 \partial \hat{\phi}_2 \right] \\ & + \int_0^L dx \left[\xi(x) e^{i(\hat{\phi}_1 + 3\hat{\phi}_2)} + H.c. \right], \end{aligned} \quad (15)$$

where we have omitted the dependence of the fields on the variable x for notational convenience. In the above Equation the bosonic field $\hat{\phi}_1(x)$ describes the charge density fluctuations of an edge state at filling factor $\nu_1 = 1$ propagating with velocity v_1 , while the field $\hat{\phi}_2(x)$ the ones of an edge state at $\nu_2 = -1/3$ (counter-propagating with respect to the previous one) with velocity v_2 . These fields satisfy the commutation relations

$$[\hat{\phi}_j(x), \hat{\phi}_k(y)] = i\pi\nu_j \delta_{j,k} \text{sgn}(x - y) \quad (j, k = 1, 2) \quad (16)$$

and are coupled by means of a short-range interaction term with intensity v_{12} . Moreover, a term describing the random tunnelling of electrons between these two edge channels with amplitude $\xi(x)$ is included. These processes are due to the presence of impurities along the edge and their role in the dynamics will be discussed in the following.

Looking more in detail into the form of the bosonic fields $\hat{\phi}_{1/2}(x)$ one has that they can be decomposed as

$$\hat{\phi}_{1/2}(x) = \hat{\phi}_{1/2}^{(p)}(x) + \hat{\phi}_{1/2}^{(0)}(x). \quad (17)$$

The first term in Eq. (17) is a plasmonic contribution

$$\hat{\phi}_{1/2}^{(p)}(x) = \sum_{k=0}^{+\infty} \sqrt{\frac{2\pi|\nu_{1/2}|}{kL}} e^{-\frac{k\alpha}{2}} \left(\hat{b}_{1/2,k} e^{ikx} + \hat{b}_{1/2,k}^\dagger e^{-ikx} \right) \quad (18)$$

which obeys the periodic boundary condition $\hat{\phi}_{1/2}^{(p)}(x+L) = \hat{\phi}_{1/2}^{(p)}(x)$. In Eq. (18) we have introduced the bosonic annihilation (creation) operator $\hat{b}_{1/2,k}$ ($\hat{b}_{1/2,k}^\dagger$), α is a short distance cut-off and where the wave-numbers are quantized according to

$$k = \frac{2\pi}{L} m, \quad (19)$$

with $m \in \mathbb{N}^*$.

The second term in Eq. (17) is a zero mode contribution

$$\hat{\phi}_{1/2}^{(0)}(x) = \pm \frac{2\pi}{L} \hat{N}_{1/2} x - \nu_{1/2} \hat{\chi}_{1/2} \quad (20)$$

where the operators $\hat{N}_{1/2}$ count the excess number of electron in the corresponding channel with respect to a given reference and $\hat{\chi}_{1/2}$ is an additional operator satisfying

$$[\hat{\chi}_j, \hat{N}_k] = i\delta_{j,k} \quad (21)$$

and such that $e^{\pm i\hat{\chi}_{1/2}}$ changes $\hat{N}_{1/2}$ by ± 1 playing the role of a Klein factor.

Combining the operators $\hat{\phi}_{1/2}$, it is possible to define the new charged ($\hat{\phi}_\rho(x)$) and neutral ($\hat{\phi}_\sigma(x)$) fields given by

$$\hat{\phi}_\rho = \sqrt{\frac{3}{2}} (\hat{\phi}_1 + \hat{\phi}_2) \quad (22)$$

$$\hat{\phi}_\sigma = \frac{1}{\sqrt{2}} (\hat{\phi}_1 + 3\hat{\phi}_2), \quad (23)$$

with

$$[\phi_{\rho/\sigma}(x), \phi_{\rho/\sigma}(y)] = \pm i\pi \text{sgn}(x-y). \quad (24)$$

According to this, one can rewrite the Hamiltonian in Eq. (15) as

$$\begin{aligned} \hat{H}_D &= \frac{1}{4\pi} \int_0^L dx \left[v_\rho (\partial_x \hat{\phi}_\rho)^2 + v_\sigma (\partial_x \hat{\phi}_\sigma)^2 + v_{\rho\sigma} \partial \hat{\phi}_\rho \partial \hat{\phi}_\sigma \right] \\ &+ \int_0^L dx \left[\xi(x) e^{i\sqrt{2}\hat{\phi}_\sigma} + H.c. \right], \end{aligned} \quad (25)$$

with

$$v_\rho = \frac{3}{2}v_1 + \frac{1}{2}v_2 - v_{12} \quad (26)$$

$$v_\sigma = \frac{1}{2}v_1 + \frac{3}{2}v_2 - v_{12} \quad (27)$$

$$v_{\rho\sigma} = -\sqrt{3}(v_1 + v_2) + \left(\sqrt{3} + \frac{1}{\sqrt{3}} \right) v_{12}. \quad (28)$$

The very remarkable fact discussed in Refs. [6,7], is that in presence of strong enough random electron tunneling $\xi(x)$ the system flows towards a fixed point with effective Hamiltonian description

$$\hat{H}_D \approx \frac{1}{4\pi} \int_0^L dx \left[v_\rho (\partial_x \hat{\phi}_\rho)^2 + v_\sigma (\partial_x \hat{\phi}_\sigma)^2 \right] \quad (29)$$

with $v_\rho \gg v_\sigma$.

This so called *disorder dominated* Hamiltonian will be the basis of following analysis. It is worth to note that, in a situation where it is possible to relax the condition of extremely precise conductance quantization, the same Hamiltonian in Eq. (25) can be derived simply assuming strong Coulomb interaction between the modes and neglecting the random electron tunneling between the channels [9]. This strengthen the generality of the following analysis.

Taking into account again the decomposition into plasmonic and zero mode part, the quantum dot Hamiltonian can be rewritten as

$$\hat{H}_D \approx \sum_{m=1}^{+\infty} m (E_\rho \hat{b}_{\rho,m}^\dagger \hat{b}_{\rho,m} + E_\sigma \hat{b}_{\sigma,m}^\dagger \hat{b}_{\sigma,m}) + \frac{3}{4} E_\rho (\hat{N}_1 - \hat{N}_2)^2 + \frac{1}{4} E_\sigma (\hat{N}_1 - 3\hat{N}_2)^2 \quad (30)$$

where we have introduced the new bosonic annihilation (creation) operators $\hat{b}_{\rho/\sigma,m}$ ($\hat{b}_{\rho/\sigma,m}^\dagger$) and defined

$$E_{\rho/\sigma} = \frac{2\pi}{L} v_{\rho/\sigma}. \quad (31)$$

Tunneling Hamiltonian

We consider now the possibility of electron tunneling from the leads to the quantum dot and viceversa. Considering only the more relevant tunneling process, it is possible to write the local tunneling Hamiltonian

$$\hat{H}_T = \sum_{l=L,R} [t_l \hat{\Psi}_l^\dagger(x_l) \hat{\Psi}_D(x_l) + t_l^* \hat{\Psi}_D^\dagger(x_l) \hat{\Psi}_l(x_l)] \quad (32)$$

with

$$\hat{\Psi}_D(x) = \frac{1}{\sqrt{2\pi\alpha}} e^{i\frac{\pi}{L}x} e^{i\hat{\phi}_1(x)} = \frac{1}{\sqrt{2\pi\alpha}} e^{i\frac{\pi}{L}x} e^{i\left[\sqrt{\frac{1}{2}}\hat{\phi}_\rho(x) - \sqrt{\frac{1}{2}}\hat{\phi}_\sigma(x)\right]} \quad (33)$$

the bosonized expression for the annihilation operator on an electron in the ν_1 channel [9], t_l the (energy independent) tunneling amplitudes and $x_{L/R}$ the points where the local tunneling occurs. Finally the additional phase factor has been introduced in order to provide the proper boundary conditions for the electron field operator on a closed geometry [10–12].

Hamiltonian of the systems

According to the above discussions the complete Hamiltonian of the system can be written as

$$\hat{H} = \hat{H}_L + \hat{H}_R + \hat{H}_D + \hat{H}_T. \quad (34)$$

This will be used in the following to evaluate the tunneling rates.

Tunneling rates

Starting from the Hamiltonian in Eq. (30), a generic state of the quantum dot can be completely characterized in terms of the quantum numbers

$$|N_1, N_2, \{n\}_\rho, \{n\}_\sigma\rangle \quad (35)$$

with N_j ($j = 1, 2$) the number of electron in the j -th channel and

$$\{n\}_{\rho/\sigma} = \{n_{\rho/\sigma,1}; n_{\rho/\sigma,2}; \dots; n_{\rho/\sigma,m}; \dots\} \quad (36)$$

the occupation numbers of the charged and neutral plasmon modes for every wave number m . Within the sequential tunneling regime, where for each tunneling process only one electron is transferred from the leads to the dot and viceversa due to the action of \hat{H}_T , eventually exciting some plasmons, these quantum numbers are enough to completely describe the transport properties of the system. Moreover, due to the form of \hat{H}_T , tunneling events can only change N_1 leaving N_2 unaffected.

Here, we assume a tunneling amplitude weak enough that the tunneling conductance remains smaller with respect to the conductance quantum e^2/h . Within this approximation we can consider the rate for the transition between an arbitrary initial state of the total system $|i\rangle$ to a final state $|f\rangle$ induced by the tunneling Hamiltonian \hat{H}_T . It can be evaluated using the Fermi's golden rule

$$\Gamma(|i\rangle \rightarrow |f\rangle) = 2\pi |\langle i | \hat{H}_T | f \rangle|^2 \delta(E_f - E_i) \quad (37)$$

with E_i (E_f) the initial (final) energy.

Integrating over the states of the electrons in the leads and taking into account the fact that they are characterized by the thermal distribution of free fermions in Eq. (13), one has that the total tunneling rates for adding or removing an electron from the channel at ν_1 of the dot through the $l = L, R$ contact can be written respectively as [13–15]

$$\begin{aligned} & \Gamma_l(N_1, N_2, \{n\}_\rho, \{n\}_\sigma \rightarrow N_1 + 1, N_2, \{n'\}_\rho, \{n'\}_\sigma) \\ &= \gamma_l \mathcal{M}(\{n\}_\rho, \{n'\}_\rho) \mathcal{M}(\{n\}_\sigma, \{n'\}_\sigma) \\ & \times f_l[\Delta_+(N_1, N_2, \{n\}_\rho, \{n\}_\sigma, \{n'\}_\rho, \{n'\}_\sigma)] \end{aligned} \quad (38)$$

and

$$\begin{aligned} & \Gamma_l(N_1, N_2, \{n\}_\rho, \{n\}_\sigma \rightarrow N_1 - 1, N_2, \{n'\}_\rho, \{n'\}_\sigma) \\ &= \gamma_l \mathcal{M}(\{n\}_\rho, \{n'\}_\rho) \mathcal{M}(\{n\}_\sigma, \{n'\}_\sigma) \\ & \times \{1 - f_l[-\Delta_-(N_1, N_2, \{n\}_\rho, \{n\}_\sigma, \{n'\}_\rho, \{n'\}_\sigma)]\}. \end{aligned} \quad (39)$$

In the above equations we have defined

$$\gamma_l = \frac{|t_l|^2}{vL} \quad (40)$$

and the matrix elements taking into account the possible change of the excitation number in the plasmon sectors are given by [15]

$$\mathcal{M}(\{n\}, \{n'\}) = \frac{\prod_{m=1}^{m_{max}} e^{-\frac{1}{2m}} \left(\frac{1}{2m}\right)^{|n_m - n'_m|} \frac{n_m^{(<)}}{n_m^{(>)}} \left[\mathcal{L}_{n_m^{(<)}}^{|n_m - n'_m|} \left(\frac{1}{2m}\right) \right]^2}{\prod_{m=1}^{m_{max}} e^{-\frac{1}{2m}}} \quad (41)$$

where

$$n_m^{(>)} = \max(n_m, n'_m) \quad (42)$$

$$n_m^{(<)} = \min(n_m, n'_m), \quad (43)$$

$\mathcal{L}_a^b(x)$ are the associated Laguerre polynomials, and m_{max} is an index such that $n_m = n'_m = 0$ for every $m > m_{max}$. Notice that, in the following, we will consider the possibility of having different values of m_{max} for charged and neutral sectors. This will allow us to consider tunneling events able to excite only the neutral sector, leaving the charged one unaffected. In the following we will demonstrate how this assumption is crucial in order to justify the experimentally observed enhancement of the Fano factor.

In Eqs. (38–39) we have also introduced the short notation

$$\begin{aligned} & \Delta_\pm(N_1, N_2, \{n\}_\rho, \{n\}_\sigma, \{n'\}_\rho, \{n'\}_\sigma) \\ &= E(N_1 \pm 1, N_2, \{n'\}_\rho, \{n'\}_\sigma) - E(N_1, N_2, \{n\}_\rho, \{n\}_\sigma) \end{aligned} \quad (44)$$

with

$$\begin{aligned}
& E(N_1, N_2, \{n\}_\rho, \{n\}_\sigma) \\
&= \frac{3}{4}E_\rho(N_1 - N_2)^2 + \frac{1}{4}E_\sigma(N_1 - 3N_2)^2 + \sum_{m=1}^{+\infty} m(E_\rho n_{m,\rho} + E_\sigma n_{m,\sigma})
\end{aligned} \tag{45}$$

in agreement with Eq. (30).

In the following, we will focus on a regime where only a limited number of tunneling rates provide a relevant contribution to the transport, the other being suppressed either by the plasmon contribution or by the energy mismatch in the Fermi distributions. In particular, we will consider a three-state model elaborated in Refs. [13,14,16] where an interaction-induced enhancement of the noise, and consequently of the Fano factor, has been reported.

Three-state model

E_σ	F
10	1.07
15	1.27
20	1.50
25	1.68
30	1.80

Table I: Fano factor for different values of E_σ (in μeV). Other parameters are: $E_\rho = 200 \mu\text{eV}$, $E_V = 50 \mu\text{eV}$ and $E_T = 9 \mu\text{eV}$.

Considering, as stated above, the symmetric voltage configurations $V_{L/R} = \pm V/2$ one can write the relevant tunneling rates

$$\begin{aligned}
\mathcal{A}_- &= \Gamma_L(0, 0, \{0\}_\rho, \{0\}_\sigma \rightarrow 1, 0, \{0\}_\rho, \{0\}_\sigma) / \gamma_L \\
&= \frac{1}{1 + \exp\left(\frac{3E_\rho + E_\sigma}{4E_T} - \frac{E_V}{2E_T}\right)}
\end{aligned} \tag{46}$$

$$\begin{aligned}
\mathcal{A}_+ &= \Gamma_R(1, 0, \{0\}_\rho, \{0\}_\sigma \rightarrow 0, 0, \{0\}_\rho, \{0\}_\sigma) / \gamma_R \\
&= \frac{\exp\left(\frac{3E_\rho + E_\sigma}{4E_T} + \frac{E_V}{2E_T}\right)}{1 + \exp\left(\frac{3E_\rho + E_\sigma}{4E_T} + \frac{E_V}{2E_T}\right)}
\end{aligned} \tag{47}$$

$$\begin{aligned}
\mathcal{B}_- &= \Gamma_L(0, 0, \{0\}_\rho, \{1\}_\sigma \rightarrow 1, 0, \{0\}_\rho, \{0\}_\sigma) / \gamma_L \\
&= \frac{1}{2} \frac{1}{1 + \exp\left(\frac{3E_\rho}{4E_T} - \frac{3E_\sigma}{4E_T} - \frac{E_V}{2E_T}\right)}
\end{aligned} \tag{48}$$

$$\begin{aligned}
\mathcal{B}_+ &= \Gamma_R(1, 0, \{0\}_\rho, \{0\}_\sigma \rightarrow 0, 0, \{0\}_\rho, \{1\}_\sigma) / \gamma_R \\
&= \frac{1}{2} \frac{\exp\left(\frac{3E_\rho}{4E_T} - \frac{3E_\sigma}{4E_T} + \frac{E_V}{2E_T}\right)}{1 + \exp\left(\frac{3E_\rho}{4E_T} - \frac{3E_\sigma}{4E_T} + \frac{E_V}{2E_T}\right)}.
\end{aligned} \tag{49}$$

In the above expressions we have introduced the short notations $E_V = eV$ and $E_T = k_B T$. Here, it is possible to highlight the role played by an unrelaxed dipolar plasmon leading to the emergence of different current-carrying processes.

Within this picture the Fano factor, namely the ratio between the current fluctuation (noise) and the current itself, can be written as [13,14,16]

$$F = 1 + 2 \left[\frac{\mathcal{A}_+ \mathcal{B}_+ (\mathcal{A}_- - \mathcal{B}_-)^2 - \mathcal{A}_- \mathcal{B}_- (\mathcal{A}_- \mathcal{B}_+ + \mathcal{A}_+ \mathcal{B}_-)}{\mathcal{A}_+ \mathcal{B}_- + \mathcal{A}_- \mathcal{B}_+ + \mathcal{A}_- \mathcal{B}_-} \right]. \quad (50)$$

This quantity is reported in Table I for different values of E_σ showing an enhancement of the Fano factor ($1 \leq F \leq 2$) as a consequence of the interaction-induced separation into a fast propagating charged mode and a slow (counter)-propagating neutral mode in a range of parameters consistent with the experimental conditions.

DETAILS OF THE THOMAS-FERMI CALCULATION

This section describes the details of our Thomas-Fermi (TF) calculation, which predicts the quantum Hall droplet reconstruction at the QPC under experimentally relevant gate geometries. We closely follow the approach developed in Ref. [1,17] and briefly review it below. The total energy of the two-dimensional electron gas is written as a functional of the electron density $n(\mathbf{r})$,

$$\mathcal{E}[n(\mathbf{r})] = \frac{e^2}{2} \int_{\mathbf{r}_1, \mathbf{r}_2} n(\mathbf{r}_1) V(\mathbf{r}_1, \mathbf{r}_2) n(\mathbf{r}_2) - e \int_{\mathbf{r}} \Phi(\mathbf{r}) + \mathcal{E}_{\text{xc}}[n(\mathbf{r})]. \quad (51)$$

Here, the first term represents electron-electron (Hartree) interactions, the second term arises from gate-induced potentials, and $\mathcal{E}_{\text{xc}}[n(\mathbf{r})]$ incorporates exchange-correlation. We adopt the local density approximation (LDA) by writing

$$\mathcal{E}_{\text{xc}}[n(\mathbf{r})] = \int_{\mathbf{r}} E_{\text{xc}}(n(\mathbf{r})), \quad E_{\text{xc}}(n) = \int_0^n dn' \mu(n'), \quad (52)$$

where $\mu(n)$ comes from our previously measured chemical potential in monolayer graphene at high magnetic field [18]. The minimization of $\mathcal{E}[n(\mathbf{r})]$ follows Ref. [1,17], with a coarse-grained treatment of $n(\mathbf{r})$ at magnetic length ℓ_B scale.

A central new ingredient, not included in Ref. [1,17], is the dielectric function $\epsilon_\nu(\mathbf{q})$ that encodes inter-Landau-level (LL) mixing at the level of random phase approximation (RPA). We implement

$$\epsilon_\nu(\mathbf{q}) = 1 - V_0(\mathbf{q}) \Pi_\nu(\mathbf{q}, \omega = 0), \quad (53)$$

where $V_0(\mathbf{q})$ is the bare Coulomb interaction, and $\Pi_\nu(\mathbf{q}, \omega = 0)$ sums over allowed LL transitions. The overall scale of $\Pi_\nu(\mathbf{q}, \omega = 0)$ depends on the fine-structure constant α_G in graphene. Previous studies place α_G in the range (1.75, 2.2) [18,19], and here we set $\alpha = 2$. This modification removes the need to artificially boost E_{xc} by a factor of 1–2 to reproduce experiments in previous works [1,17].

We simulate a system at $B = 13$ T (magnetic length $\ell_B \approx 7$ nm), with a top gate at $d_t = 60$ nm, a back gate at $d_b = 30$ nm, and channel widths $w_{\text{EW}} = w_{\text{NS}} = 30$ nm. The hBN between gates and sample has anisotropic dielectric constants $\epsilon_{\parallel} = 6.6$ and $\epsilon_{\perp} = 3$. We discretize a $60 \ell_B \times 60 \ell_B$ region into grid spacing $\Delta x = \Delta y = \ell_B/5$. In momentum space, the gate-screened Coulomb kernel is

$$V(\mathbf{q}) = \frac{e^2}{4\pi\epsilon_0} \frac{4\pi \sinh(\beta d_t |\mathbf{q}|) \sinh(\beta d_b |\mathbf{q}|)}{\sinh[\beta(d_t + d_b)|\mathbf{q}||\mathbf{q}|]} \frac{|F_N(\mathbf{q})|^2}{\epsilon_{\text{hBN}} \epsilon_\nu(\mathbf{q})}, \quad (54)$$

where $\beta = \sqrt{\epsilon_{\parallel}/\epsilon_{\perp}}$, $\epsilon_{\text{hBN}} = \sqrt{\epsilon_{\parallel}\epsilon_{\perp}}$, and $F_N(\mathbf{q})$ the usual LL form factor. For the zero energy LL in graphene, $F_0(\mathbf{q}) = e^{-\frac{1}{4}|\mathbf{q}|^2 \ell_B^2}$. We further tune the gate voltages to fix the filling factor $\nu_{\text{EW}} = 2$ beneath the east and west gates and $\nu_{\text{NS}} = 0$ beneath the north and south gates, which follows experiment and creates a QPC region with $1 \lesssim \nu \lesssim 2$. We find both the filling factors $\nu_{\text{NS}} = 0$ and $\Pi_\nu(\mathbf{q}, \omega = 0)$ crucial to reproduce the reconstructed islands anticipated at the QPC.

RECONSTRUCTION AT THE QPC

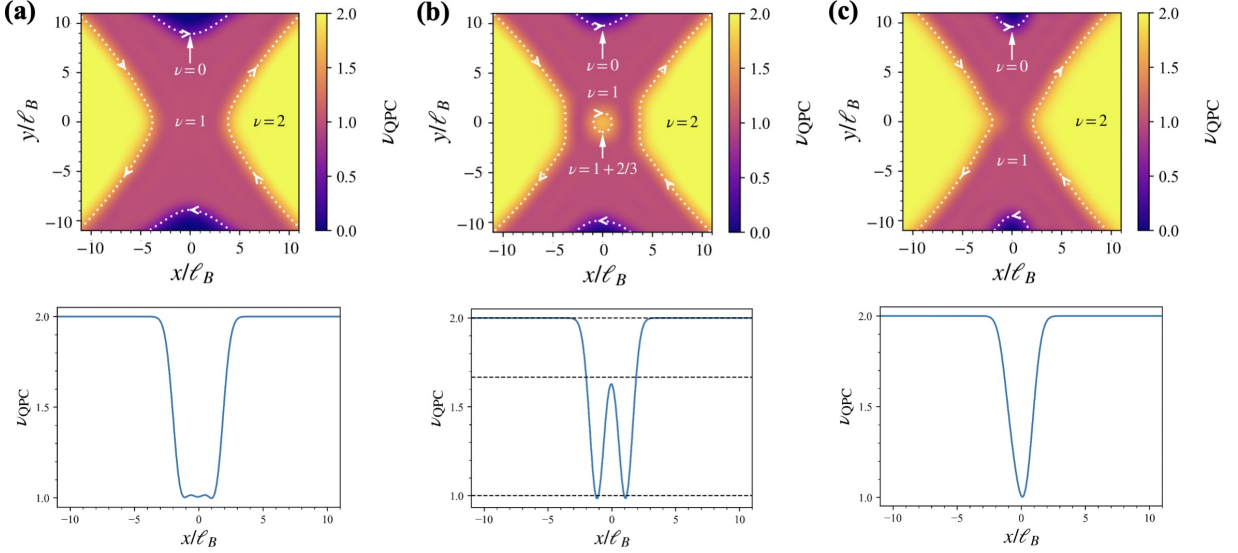
In Ref. [17], a Thomas-Fermi calculation similar to the one presented here demonstrated that a fractional island with filling $\nu = 1/3$ can appear at the saddle point of a QPC, provided the confining potential is sufficiently smooth compared to the Coulomb energy. In the present work, which focuses on a different bulk filling configuration ($\nu_{\text{EW}} = 2$

and $\nu_{\text{NS}} = 0$), we find that a similar reconstruction takes place at the QPC but instead yields an isolated quantum dot at $\nu = 2/3$. This observation underpins the noise model discussed in the main text.

The reconstruction is governed by the competition between two energy scales: the Coulomb energy E_C and the confining-potential scale E_V . Concretely,

$$E_C = \frac{e^2}{4\pi\epsilon_0\epsilon_{\text{hBN}}\ell_B} \approx 47.4 \text{ meV}, \quad E_V = e \left(\frac{\partial\Phi}{\partial r} \right) \ell_B. \quad (55)$$

Here, E_C sets the characteristic Coulomb strength in the system, while E_V measures how quickly the electrostatic potential varies across the magnetic length ℓ_B . Generally, a smaller ratio E_V/E_C favors the formation of reconstructed islands. By tuning gate voltages $V_{\text{EW}}, V_{\text{NS}}, V_{\text{B}}$, we access $E_V/E_C \in [0.57, 0.61]$.



Supplemental Figure 15: Reconstructed two-dimensional electron density profiles in a QPC geometry, along with one-dimensional cuts in the x -direction, for different values of E_V/E_C . (a) At $E_V/E_C = 0.57$, there is a relatively wide $\nu = 1$ channel beneath the E/W gates ($\nu_{\text{EW}} = 2$), with no localized dot. (b) Increasing to $E_V/E_C = 0.59$ produces an island at the QPC center with $\nu = 2/3$ (above the $\nu = 1$ plateau). (c) Further increasing to $E_V/E_C = 0.61$ narrows the $\nu = 1$ channel until the fractional dot disappears.

Figure 15 illustrates our main findings. We keep $\nu_{\text{EW}} = 2$ under the EW gates and $\nu_{\text{NS}} = 0$ under the NS gates, while varying E_V/E_C . When $E_V/E_C = 0.57$, the $\nu = 1$ channel is wide, and no localized state forms above $\nu = 1$. As E_V/E_C increases to 0.59, a fractional island appears at $\nu = 2/3$. This differs from the $\nu = 1/3$ droplet in Ref. [17] due to the changed bulk filling ($\nu_{\text{NS}} = 0$). Finally, at $E_V/E_C = 0.61$, the channel narrows enough that the $\nu = 2/3$ island vanishes, leaving a simpler edge structure.

In addition to requiring a suitable E_V/E_C ratio, the formation of the $\nu = 2/3$ island also depends on the width of the $\nu = 1$ channel. If this channel is too narrow for a given E_V/E_C , the island cannot emerge; conversely, if it is too wide, the potential gradient is insufficient to confine electrons above $\nu = 1$. Consequently, both the slope of the confining potential and the $\nu = 1$ channel width work together to determine whether the fractional droplet materializes in the QPC region.

The fractional $\nu = 2/3$ island encloses two $\nu = 1/3$ edge channels, which can recombine into a charge mode and a neutral mode upon hybridization. This neutral mode could mediate tunneling between the $\nu = 2$ bulk edges and the island's charge mode, and therefore enhance current fluctuations at the QPC. Consequently, the emergence of this fractional droplet is consistent with the observed noise signatures in our experiment.

SEMICLASSICAL MODEL

The code of the semiclassical model is shown below. It consists in building charge transfer statistics over a large number of tunneling attempts, with a simple rule: whenever a tunneling attempt (parametrized in the code by the transmission probability t) is successful, the next attempt automatically succeeds. After this dual tunneling process

the transmission probability is reset back to t . We compute the reflected current as the average number of failed attempts and its noise as the variance, yielding the Fano factor calculation shown in main text Fig. 3 and Supplemental Fig. 11.

* Equal contribution.

† Equal contribution. Contact: olivier.maillet@cea.fr

‡ Contact: preden.roulleau@cea.fr

§ Contact: francois.parmenier@phys.ens.fr

- [1] L. A. Cohen, N. L. Samuelson, T. Wang, K. Klocke, C. C. Reeves, T. Taniguchi, K. Watanabe, S. Vijay, M. P. Zaletel, and A. F. Young, Nanoscale electrostatic control in ultraclean van der waals heterostructures by local anodic oxidation of graphite gates, *Nature Physics* **19**, 1502 (2023).
- [2] G. L. Breton, R. Delagrangé, Y. Hong, M. Garg, K. Watanabe, T. Taniguchi, R. Ribeiro-Palau, P. Roulleau, P. Roche, and F. Parmentier, Heat equilibration of integer and fractional quantum hall edge modes in graphene, *Physical Review Letters* **129**, 116803 (2022).
- [3] R. Delagrangé, M. Garg, G. L. Breton, A. Zhang, Q. Dong, Y. Jin, K. Watanabe, T. Taniguchi, P. Roulleau, O. Maillet, P. Roche, and F. D. Parmentier, Vanishing bulk heat flow in the $\nu = 0$ quantum hall ferromagnet in monolayer graphene, *Nature Physics* **20**, 1927 (2024).
- [4] Y. Blanter and M. Büttiker, Shot noise in mesoscopic conductors, *Physics Reports* **336**, 1 (2000).
- [5] M. Johnson and A. MacDonald, Composite edges in the $\nu = 2/3$ fractional quantum hall effect, *Physical Review Letters* **67**, 2060 (1991).
- [6] C. L. Kane, M. P. A. Fisher, and J. Polchinski, Randomness at the edge: Theory of quantum hall transport at filling $\nu = 2/3$, *Physical Review Letters* **72**, 4129 (1994).
- [7] C. L. Kane and M. P. A. Fisher, Impurity scattering and transport of fractional quantum hall edge states, *Physical Review B* **51**, 13449 (1995).
- [8] J. Park, Y. Gefen, and H.-S. Sim, Topological dephasing in the $\nu = 2/3$ fractional quantum hall regime, *Physical Review B* **92**, 245437 (2015).
- [9] X.-G. Wen, Topological orders and edge excitations in fractional quantum hall states, *Advances in Physics* **44**, 405 (1995).
- [10] M. R. Geller and D. Loss, Aharonov-bohm effect in the chiral luttinger liquid, *Physical Review B* **56**, 9692 (1997).
- [11] A. Braggio, J. König, and R. Fazio, Full counting statistics in strongly interacting systems: Non-markovian effects, *Physical Review Letters* **96**, 026805 (2006).
- [12] M. Merlo, A. Braggio, N. Magnoli, and M. Sassetti, Transport of fractional hall quasiparticles through an antidot, *Physical Review B* **75**, 195332 (2007).
- [13] J. U. Kim, J. M. Kinaret, and M.-S. Choi, Shot noise enhancement from non-equilibrium plasmons in luttinger liquid junctions, *Journal of Physics: Condensed Matter* **17**, 3815 (2005).
- [14] J. U. Kim, M.-S. Choi, I. V. Krive, and J. M. Kinaret, Nonequilibrium plasmons and transport properties of a double-junction quantum wire, *Low Temperature Physics* **32**, 1158 (2006).
- [15] G. A. Frigeri and B. Rosenow, Electron pairing in the quantum hall regime due to neutralon exchange, *Physical Review Research* **2**, 043396 (2020).
- [16] F. Cavaliere, A. Braggio, M. Sassetti, and B. Kramer, Spin effects in transport through non-fermi-liquid quantum dots, *Physical Review B* **70**, 125323 (2004).
- [17] L. A. Cohen, N. L. Samuelson, T. Wang, K. Klocke, C. C. Reeves, T. Taniguchi, K. Watanabe, S. Vijay, M. P. Zaletel, and A. F. Young, Spontaneous Localization at a Potential Saddle Point from Edge State Reconstruction in a Quantum Hall Point Contact, *Phys. Rev. Lett.* **134**, 076302 (2025).
- [18] F. Yang, A. A. Zibrov, R. Bai, T. Taniguchi, K. Watanabe, M. P. Zaletel, and A. F. Young, Experimental Determination of the Energy per Particle in Partially Filled Landau Levels, *Phys. Rev. Lett.* **126**, 156802 (2021).
- [19] K. Shizuya, Electromagnetic response and effective gauge theory of graphene in a magnetic field, *Phys. Rev. B* **75**, 245417 (2007).

```

rng = np.random.default_rng(12349)
Result_Moy=np.array([])
Result_Sig=np.array([])
Result_Sig2=np.array([])
Final_data=np.zeros((40,3))
Final_data2=np.zeros((40,3))
Itot = 2000 #number of repetitions of a single realization
Jtot = 1000 #number of charge tunneling attempts for a single realization
# the higher Itot and Jtot, the more precise the result
print(time.asctime())
for tn in range(1,11):
    t=tn*0.1 #dot transmission, ranging between 0 and 1, in steps of 0.1
    Data=np.array([])
    for i in range(0,Itot):
        N=0 # final value of N is the number of charges that have been reflected by the dot
        Exc=0 # initializing the dot excitation
        Exc0=0 # initializing the dot excitation
        for j in range (0,Jtot):
            tfloat=rng.random() #random number for each attempt
# tfloat is compared with the dot transmission to determine the outcome of a single tunneling attempt
            if Exc0 == 0 : #no excitation in the dot
                if tfloat < t : # attempt has failed: the charge is reflected
                    N=N+1 # the number of charge having been reflected increases by 1
                else : # attempt is successful: the charge is transmitted
                    Exc=1 # the charge is transmitted through the dot and leaves an excitation, N is not changed
            if Exc0 == 1 :
#the excitation in the dot changes the tunneling probability for this attempt to 1 (thus N is not changed)
                Exc=0 #desexcitation of the dot
                Exc0=Exc # the state of the dot is reinitialized according to the latest tunneling event
            Data=np.append(Data,N) #for each repetition of a single realization, we compute N

        Sigma = np.var(Data)/np.mean(Data) # Fano factor for channel 1
        Sigma2 = np.var(Data)/(Jtot+np.mean(Data)) #Fano factor for channel 2
        Mean =np.mean(Data)/Jtot #average transmission

    Result_Moy=np.append(Result_Moy,Mean)
    Result_Sig=np.append(Result_Sig,Sigma)
    Result_Sig2=np.append(Result_Sig2,Sigma2)

    Final_data[tn-1,0]=t
    Final_data[tn-1,1]=np.mean(Data)/Jtot
    Final_data[tn-1,2]=np.var(Data)/np.mean(Data)

    Final_data2[tn-1,0]=t+1
    Final_data2[tn-1,1]=np.mean(Data)/Jtot+1
    Final_data2[tn-1,2]=np.var(Data)/(Jtot+np.mean(Data))

print(t,np.mean(Data)/Jtot,np.var(Data)/np.mean(Data),time.asctime())

```